Bull Volcanol (2011) 73:295–320
DOI 10.1007/s00445-010-0417-0

RESEARCH ARTICLE

The Averno 2 fissure eruption: a recent small-size explosive event at the Campi Flegrei Caldera (Italy)

Mauro Antonio Di Vito · Ilenia Arienzo · Giuseppe Braia · Lucia Civetta · Massimo D'Antonio · Valeria Di Renzo · Giovanni Orsi

Received: 7 August 2009 / Accepted: 19 September 2010 / Published online: 8 October 2010

Abstract The Averno 2 eruption (3,700±50 a B.P.) was an explosive low-magnitude event characterized by magmatic and phreatomagmatic explosions, generating mainly fall and surge beds, respectively. It occurred in the Western sector of the Campi Flegrei caldera (Campanian Region, South Italy) at the intersection of two active fault systems, oriented NE and NW. The morphologically complex crater area, largely filled by the Averno lake, resulted from vent activation and migration along the NE-trending fault system. The eruption generated a complex sequence of pyroclastic deposits, including pumice fall deposits in the lower portion, and prevailing surge beds in the intermediate-upper portion. The pyroclastic sequence has been studied through stratigraphical, morphostructural and petrological investigations, and subdivided into three members named A through C. Member A was emplaced during the first phase of the eruption mainly by magmatic explosions which generated columns reaching a maximum height of 10 km. During this phase the eruption reached its climax with a mass discharge rate of 3.2 10^6 kg/s. Intense fracturing and fault activation favored entry of a significant amount of water into the system, which produced explosions driven by variably efficient water-magma interaction. These explosions generated wet to dry surge deposits that emplaced Member B and C, respectively. Isopachs and isopleths maps, as well as areal distribution of ballistic fragments and facies variation of surge deposits allow definition of four vents that opened along a NE oriented, 2 km long fissure. The total volume of magma extruded during the eruption has been estimated at about 0.07 km^3 (DRE). The erupted products range in composition from initial, weakly peralkaline alkali-trachyte, to last-emplaced alkali-trachyte. Isotopic data and modeling suggest that mixing occurred during the Averno 2 eruption between a more evolved, less radiogenic stored magma, and a less

Editorial responsibility: R. Cioni

M. A. Di Vito (✉) · I. Arienzo · L. Civetta · M. D'Antonio · V. Di Renzo · G. Orsi
sezione di Napoli Osservatorio Vesuviano,
Istituto Nazionale di Geofisica e Vulcanologia,
via Diocleziano 328,
80124 Naples, Italy
e-mail: mauro.divito@ov.ingv.it

I. Arienzo
e-mail: ilenia.arienzo@ov.ingv.it

L. Civetta
e-mail: lucia.civetta@ov.ingv.it

M. D'Antonio
e-mail: masdanto@unina.it

V. Di Renzo
e-mail: valeria.direnzo@ov.ingv.it

G. Orsi
e-mail: giovanni.orsi@ov.ingv.it

G. Braia
Dipartimento Geomineralogico,
Università di Bari,
Bari, Italy
e-mail: giusbraia@yahoo.it

L. Civetta
Dipartimento di Scienze Fisiche,
Università di Napoli "Federico II",
Naples, Italy

M. D'Antonio
Dipartimento di Scienze della Terra,
Università di Napoli "Federico II",
Naples, Italy

evolved, more radiogenic magma that entered the shallow reservoir to trigger the eruption. The early phases of the eruption, during which the vent migrated from SW to the center of the present lake, were fed by the more evolved, uppermost magma, while the following phases extruded the less evolved, lowermost magma. Integration of the geological and petrological results suggests that the Averno 2 complex eruption was fed from a dyke-shaped shallow reservoir intruded into the NE-SW fault system bordering to the west the La Starza resurgent block, within the caldera floor.

Keywords Campi Flegrei caldera · Averno · Chemostratigraphy · Isotope geochemistry · Magma mixing · Eruption dynamics

Introduction

Definition of the stratigraphic sequence of the products of an eruption and their characteristics, as well as determination of their vertical and horizontal extents, and sedimentological, and lithofacies variation, provides the necessary basis for volcanological and petrological studies. Furthermore, reconstruction of the structural evolution and setting of a volcano, including reconstruction of its eruptive history and the structure of its magmatic feeding system at the time, allow interpretation of the relationships among deformation history, vent location, eruption dynamics, magma compositions, and withdrawal dynamics (e.g. Orsi et al. 1995; Schmitz and Smith 2004; Tonarini et al. 2009). In addition, definition of the emplacement mechanisms and areal distribution of different deposits permits evaluation of the impact of past eruptions.

The Campi Flegrei caldera is an active volcano as shown by the last eruption of 1,538 AD, and by recent episodes of both major (1969–72 and 1982–84) and minor (1989, 1994, 2000 and 2006) unrest, seismicity, and intense fumarolic and hot springs activity (Caliro et al. 2007 and references therein). Since the caldera and its surroundings are inhabited by more than 1.5 million people, the volcanic risk is very high (Orsi et al. 2004). In such a framework, defining the style and size of past eruptions and related hazards is crucial in order to reach the goal of forecasting eruptive scenarios. Orsi et al. (2009) considered a low-magnitude eruption as the most probable explosive event at Campi Flegrei caldera if volcanism is renewed in the short to middle term. The authors of this paper have suggested the Averno 2 (3,700±50 a b.p., Alessio et al. 1971) and Monte Nuovo (1,538 AD) eruptions as reference events for such an eruption in order to develop risk mitigation actions. This conclusion was based on both the volcanic and deformation history of the caldera, and on statistical analysis of physical parameters for the eruptions since 5 ka (Orsi et al. 1996, 1999a, 2004; Di Vito et al. 1999; Mastrolorenzo et al. 2008; Costa et al. 2009).

Although the Averno 2 eruption has been studied by many authors (Di Girolamo et al. 1984; Rosi and Sbrana 1987; Lirer et al. 1990; Mastrolorenzo 1994), current knowledge of its history and dynamics is still insufficient to define possible scenarios of a future eruption. We carried out geomorphological, structural, volcanological, petrographic, geochemical and isotopical investigations in order to reconstruct in detail the history and dynamics of the eruption, morphological and structural evolution of the vent, characteristics of the magmatic feeding system, and more generally to better define the expected characteristics of a future low-magnitude eruption.

The Campi Flegrei caldera and its magmatic feeding system

The Campi Flegrei caldera is one of the three active volcanoes in the Neapolitan area (Orsi et al. 2003; Santacroce et al. 2003). It is a nested and resurgent structure (Orsi et al. 1992, 1996) formed during two main collapses related to eruptions of the Campanian Ignimbrite (CI; 39 ka; Barberi et al. 1978; Fisher et al. 1993; Rosi et al. 1996, 1999; Civetta et al. 1997; De Vivo et al. 2001; Fedele et al. 2002, 2003, 2008; Pappalardo et al. 2002a; Ort et al. 2003) and the Neapolitan Yellow Tuff (NYT; 15 ka; Orsi et al. 1992, 1995; Scarpati et al. 1993; Wohletz et al. 1995; Deino et al. 2004) (Fig. 1a). Since 15 ka, the caldera has been the site of very intense and closely interrelated volcanism and deformation (Di Vito et al. 1999; Orsi et al. 1999a, 2004). Volcanism was mostly concentrated in three epochs of intense activity (15.0-9.5, 8.6-8.2, 4.8-3.8 ka) with the last eruption (Monte Nuovo; Di Vito et al. 1987, 1999; D'Oriano et al. 2005; Piochi et al. 2005) in 1,538 AD. Deformation, mostly related to resurgence of the central sector of the NYT caldera floor, occurred mainly along fault systems trending NE-SW, NW-SE, and subordinately N-S. During the I and II epochs, magmas reached the surface through the marginal faults of the NYT caldera and generated explosive eruptions. During the III epoch, 21 explosive and 3 effusive eruptions took place mostly in the NE sector of the caldera floor (Fig. 1a). Only the Averno 1 and Averno 2 eruptions and, more recently, the Monte Nuovo eruption, took place in the northwestern sector of the caldera, where the NE-SW San Vito-Averno fault system downthrows the La Starza block towards the NW, and likely intersects the NW-SE fault system of Pozzuoli bay (Orsi et al. 1996; Di Vito et al. 1999). These fault systems are still active and

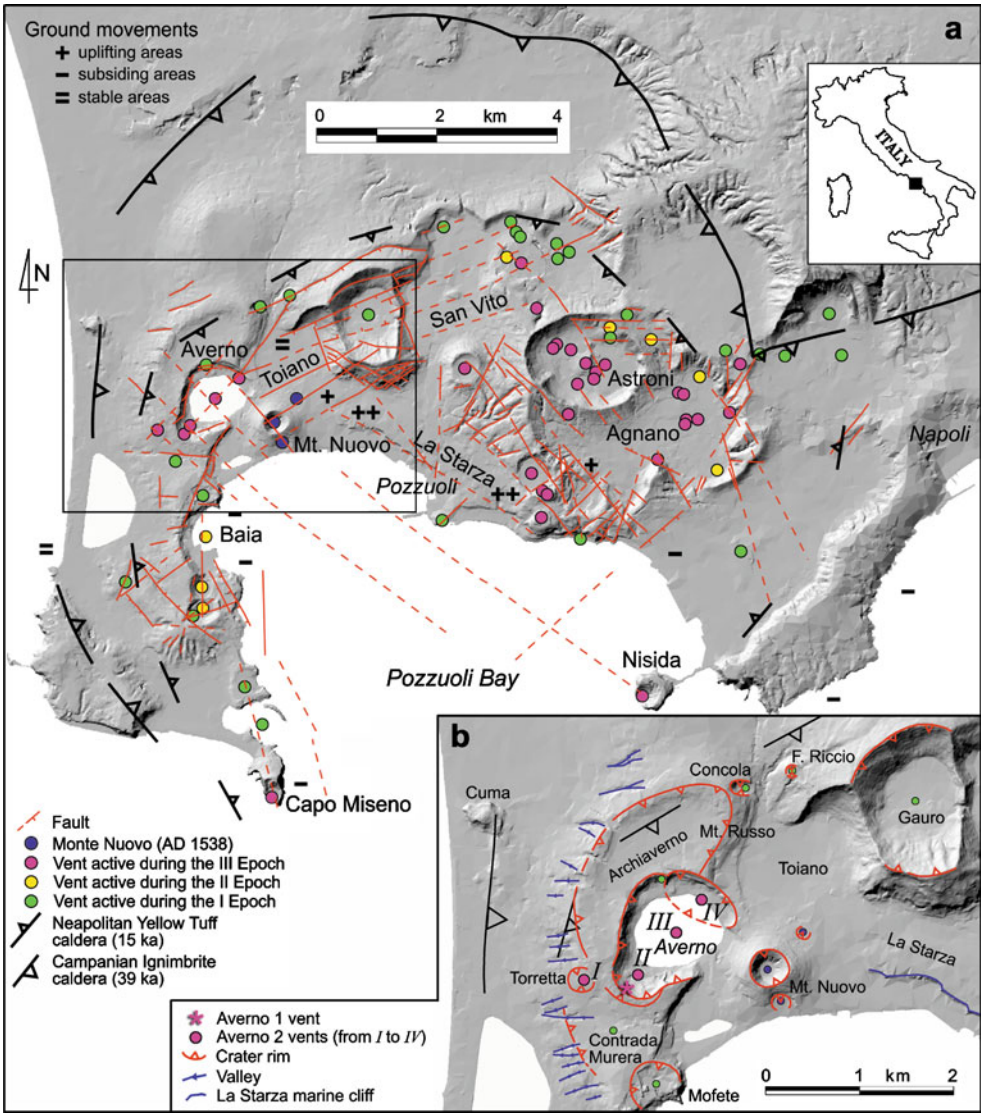

Fig. 1 **a** Campi Flegrei caldera structural sketch map (modified after Orsi et al. 2004); **b** Morpho-structural sketch map of the Averno area, delimited with the black frame in a

affected the ground deformation pattern during recent bradyseismic episodes (Orsi et al. 1999a). On the basis of the distribution of vents formed since 5 ka and the dynamics of the Campi Flegrei caldera, Orsi et al. (2004) and Selva et al. (2010) have concluded that the Averno-Monte Nuovo area, after the Agnano-San Vito one, is the second most likely site for a possible future vent opening. Averno 2 was the largest magnitude eruption in the Averno-Monte Nuovo area (Orsi et al. 2004, 2009 and references therein).

The Phlegraean magmas range in composition from shoshonite to phonolite, with a predominance of trachyte and phonolite (e.g. D'Antonio et al. 2007 and references therein). They are characterized by a relatively wide range in $^{87}Sr/^{86}Sr$ (0.7068–07086), and limited variations in $^{143}Nd/^{144}Nd$ (0.51240–0.51254) (e.g. Civetta et al. 1997; D'Antonio et al. 1999, 2007; Pappalardo et al. 2002b; Tonarini et al. 2004, 2009; Arienzo et al. 2009). Studies of melt inclusions in minerals from pumice clasts of CI and deposits younger than 15 ka suggest crystallization depths between 9 and 7 km, and 8 and 2 km for shoshonitic to trachytic, and trachytic to trachy-phonolitic magmas, respectively (Marianelli et al. 2006; Mangiacapra et al. 2008; Arienzo et al. 2010).

These results as well as geophysical data (Zollo et al. 2008 and references therein), suggest that since 10 ka the Campi Flegrei caldera's magmatic system has been characterized by deep (≈ 8 km) and shallow reservoirs. The eruptions have been fed by small magma batches rising from the shallow portion of the system. The extruded magmas generally result from mingling/mixing before and/or during eruptions of variable melts (e.g., de Vita et al.

1999; Morgan et al. 2004; Arienzo et al. 2009; Tonarini et al. 2009; Di Renzo et al. 2010).

Geological and morpho-structural features of the Averno area

Interpretation of aerial photographs, together with field investigations (see Appendix), permit recognition of the main morphological and structural features of the Averno area (Fig. 1b), although it has been intensely excavated and urbanized since Greek and Roman times (Orsi et al. 2003). The most significant geomorphic features include high-angle scarps, variably preserved volcanic edifices, lowlands and coastal and marine landforms, and features related to faults and fractures.

The Averno 2 volcano (Fig. 1b) grew among the Contrada Murera, Mofete, Gauro, Archiaverno, and Concola-Fondo Riccio edifices, formed during activity of epoch I (15.0–9.5 ka). The only other eruption that occurred during activity of epoch III in the Averno area is Averno 1, a low magnitude explosive event (Orsi et al. 2009) that formed a small edifice, later covered by the products of the Averno 2 eruption (Di Vito et al. 1999). The slopes of these volcanic cones are cut by valleys, often structurally controlled.

The fault systems in the area trend dominantly NE-SW and NW-SE, and subordinately EW and NS. These fault systems, detected throughout the Campi Flegrei caldera, have been active during caldera collapses, block resurgence and recent caldera floor activity (Cosentino et al. 1984; Orsi et al. 1996, 1999a, b; Di Vito et al. 1999). The Averno area is located to the W of the resurgent block, at the intersection of the two major fault systems, which were mainly active prior to the Averno 2 eruption, as their scarps are draped by the Averno 2 Tephra. Faults and fractures younger than the eruption were recognized in the Averno lake and Monte Nuovo areas.

The Averno area includes coastal and inland plains, a few meters above sea level and filled with marine and coastal sediments, mainly laid down during the last marine ingression at Campi Flegrei (between 8.0 and 4.0 ka) (Di Vito et al. 1999). Changes in elevation of these sediments since their emplacement have been used to evaluate the local net vertical deformation of the Campi Flegrei coastal area (Orsi et al. 1996; Di Vito et al. 1999). The Cuma plain has not been affected by detectable vertical movements, at least since Roman times, whereas the elevation of the marine sediment surface in the Toiano plain progressively increases towards the La Starza marine terrace. The terrace is displaced along a NE-SW oriented fault system (Fig. 1b) that defines the north-western margin of the La Starza block, and affects the Averno-Monte Nuovo area.

The Averno lake area, previously considered the only vent of the Averno 2 eruption (Rosi and Sbrana 1987; Mastrolorenzo 1994), has an irregular shape with steep internal slopes and flat or low-angle external slopes. In the Torretta area, south-west of the lake (Fig. 1b), these external slopes are buried under a small cone-shaped edifice composed of Averno 2 products. The internal slopes are rectilinear in the western, southern and northern sectors, whereas they are concave SW and NE of the lake (Fig. 1b). These two concave features associated with rims (*II* and *IV* in Fig. 1b) indicate craters smaller than the present lake.

The concave southwestern sector is a gentle slope, overlapping the Averno 1 vent area, completely draped by pyroclastic surge deposits of the Averno 2 Tephra, whereas the northeastern one includes high angle scarps, and is elliptically elongate along a NW-SE trend. The rectilinear sectors, as suggested by the presence of faults and fractures parallel to the present crater rim, and an alignment of triangular facets along the northwestern sector, probably resulted from late and progressive faulting due to gravitational instability of the crater slopes towards the lake area. Along all the inner slopes, except those of the SW sector, thick and almost complete sequences of the Averno 2 Tephra are exposed along with Averno 1, Fondi di Baia and Archiaverno Tephras. The attitude of these sequences varies from sub-horizontal to low-angle (Di Vito et al. 1999). The inner slopes are connected to the lake by a continuous, low-angle talus resulting from their progressive erosion. Overall, the geomorphic data suggest that the Averno 2 edifice was a complex structure with multiple active vents, resulting from an eruption more complex than previously realized (Di Girolamo et al. 1984; Rosi and Sbrana 1987; Lirer et al. 1990; Mastrolorenzo 1994).

The Averno 2 Tephra

The Averno 2 Tephra (AV2T), a complex pyroclastic sequence composed of pyroclastic-fall and -density current (pdc) deposits, has been studied by many authors (De Lorenzo 1904; Rittmann 1950; Scherillo and Franco 1960; Di Girolamo et al. 1984; Rosi and Sbrana 1987; Lirer et al. 1990; Mastrolorenzo 1994). It overlies a thick paleosol, dated at 3,700±50 a (Alessio et al. 1971), developed on the Averno 1 Tephra (4,530±50 a; Di Vito et al. 1999), and locally a few cm thick paleosol, developed on Unit 7 of the Astroni volcano (3,820±50 a, Di Vito et al. 1999; Isaia et al. 2004; Tonarini et al. 2009). New stratigraphic data presented in Fig. 2 (methods in Appendix) show that AV2T underlies the Phlegraean Fossa Lupara Tephra in the Monte Russo area, from which it is separated by a thin paleosol. Finally the AV2T underlies the Monte Nuovo Tephra, the product of the only historical eruption of Campi Flegrei

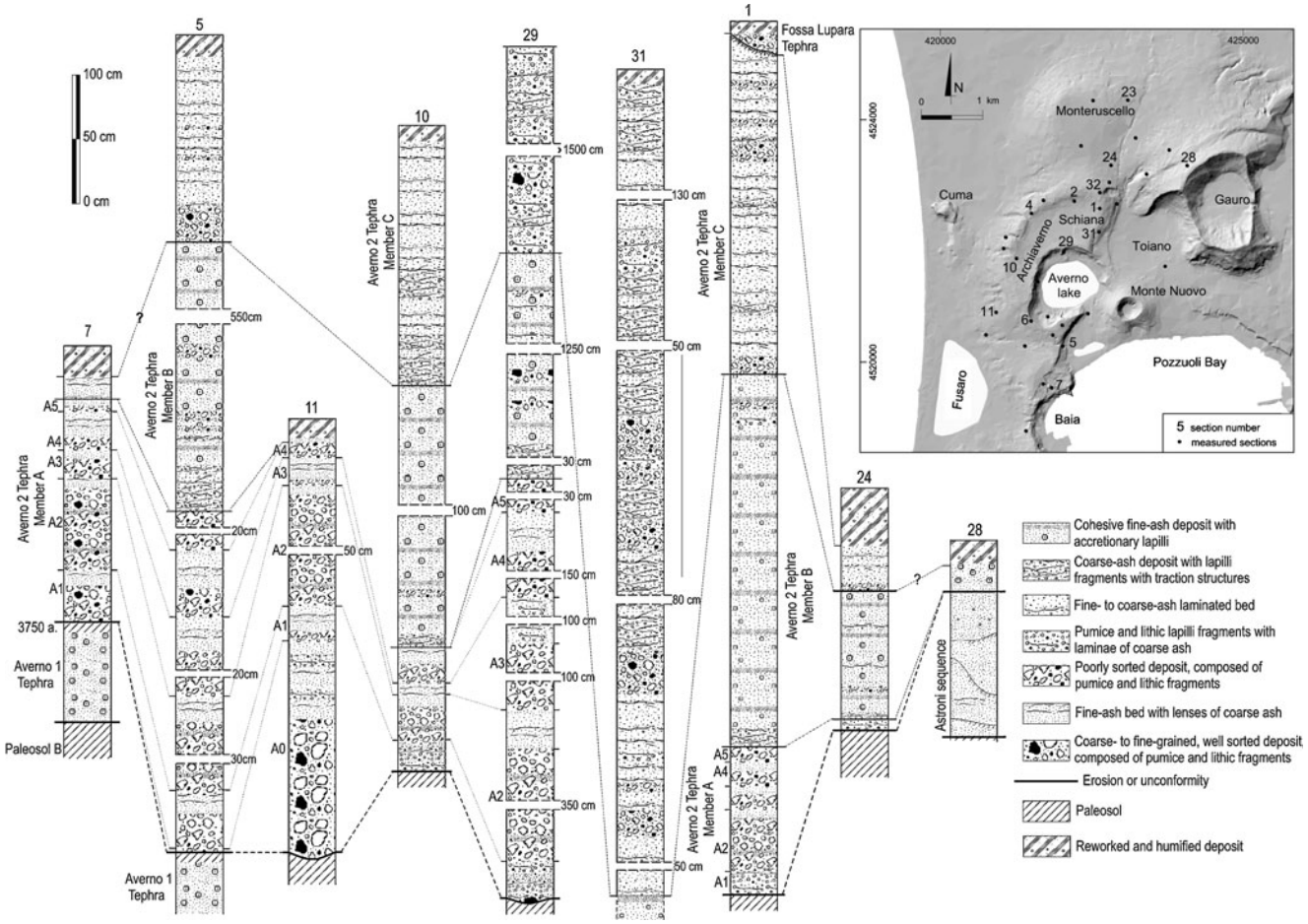

Fig. 2 Measured stratigraphic sections of the Averno 2 Tephra (*dots on the map*). Numbers indicate the exposures selected for stratigraphic correlations or rock sampling

(1,538 AD), from which it is separated by a well developed paleosol that locally contains pottery and marble fragments of Roman and Medieval times (Gialanella, pers. com.). In the Monte Nuovo area, the AV2T has been cored directly above shallow-sea sediments (Di Vito et al. 1999).

AV2T is the most widespread pyroclastic sequence among those erupted in the western sector of the Campi Flegrei caldera since 5,000 years ago (Rosi and Sbrana 1987; Di Vito et al. 1999; Orsi et al. 2004, 2009; Costa et al. 2009). Fall layers dominate the lower portion of the sequence, while surge beds, generated by wet and dry pyroclastic density currents during the eruption, prevail upsection. The entire sequence has been subdivided into three members, A through C from base upsection, based on their lithological and sedimentological characteristics and described in detail in Figs. 2, 3, 4 and 5 (field and analytical methods are reported in Appendix). Figure 3 describes the main lithological, sedimentological, morphologic and mineralogical characteristics of each member and sub-member. SEM analyses (Figs. 3 and 6) have been carried out on about 100 ash particles for each sample, representing all the recognized members and sub-members (for details see Appendix). On the basis of the main lithological and morphological features, the ash particles, including juvenile and lithic components, have been grouped into 3 types. With reference to previous studies (Büttner et al. 2002; Dellino et al. 2001; Dellino and La Volpe 1995; Heiken 1974; Heiken and Wohletz 1985; Palladino et al. 2008), the characteristics of the juvenile fragments have been used to infer the dominant fragmentation process (magmatic/phreatomagmatic). Highly vesicular, fresh fragments, sometimes affected by plastic deformation, with ovoid to elongated vesicles, have been interpreted as the product of magmatic fragmentation (type 1 in Fig. 3). Blocky and equant fragments, with quench cracks and/or stepped surfaces (type 2a in Fig. 3), as well as fragments with pitted surfaces, adhering particles or alteration skins (type 2b in Fig. 3), have been attributed to phreatomagmatic fragmentation.

Member A This Member includes 6 sub-members, A0 through A5 (Fig. 3), each composed of a sequence of fall deposits overlain by surge beds. It is covered by a widely distributed coarse-ash bed predating the phreatomagmatic

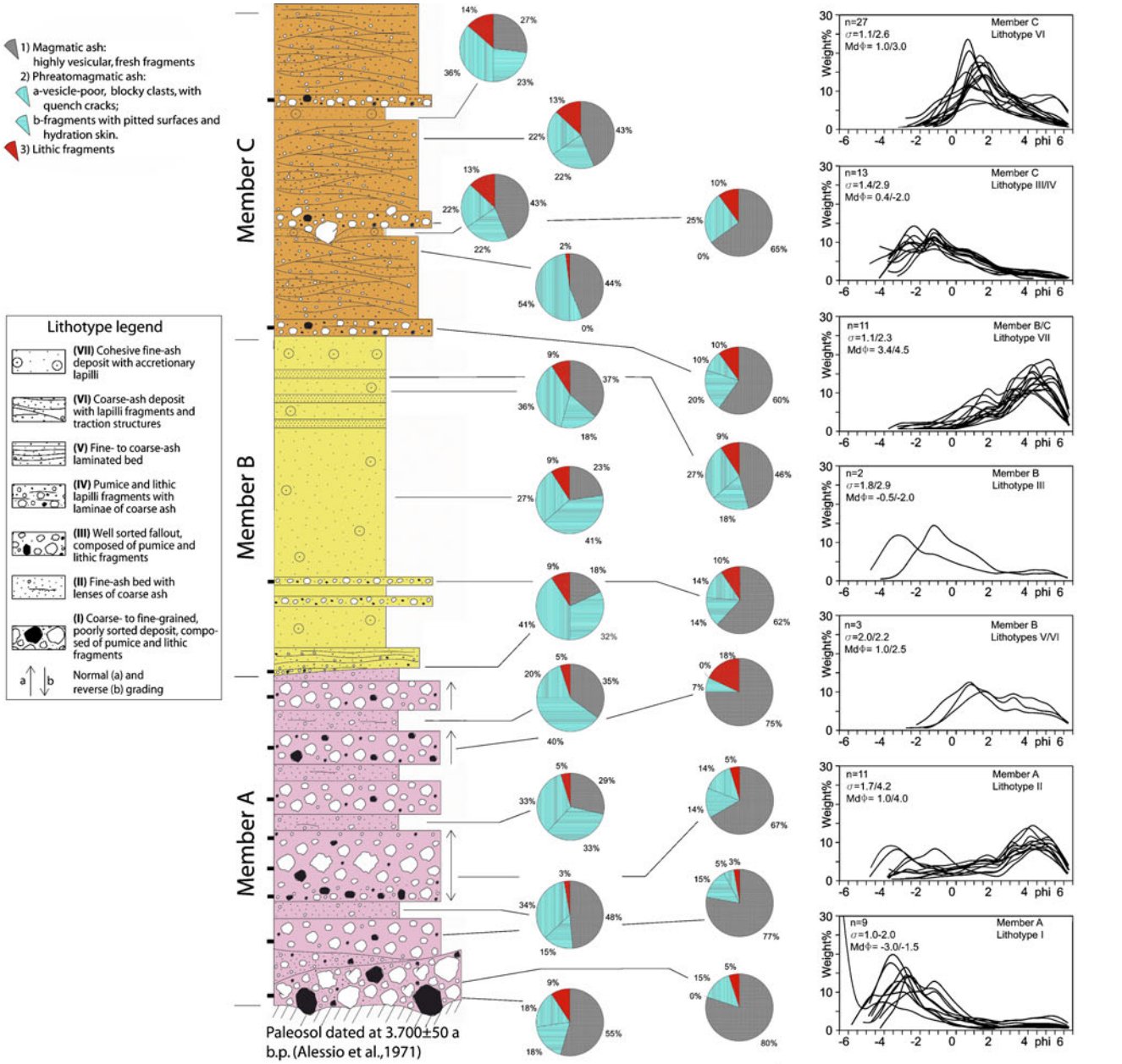

Member C: Sequence of prevailing dry surge beds and minor fall deposits. The volume of magma is 0.025 km^3 (D.R.E.). Succession of cross-laminated, coarse- to fine-ash surge beds and minor, poorly sorted lapilli-sized pumice fallout layers and thin, gray to purple, accretionary lapilli-rich, fine-ash beds. In proximal exposures the fallout beds are partially eroded by surges and locally form traction carpet structures. Pumice fragments are generally porphyritic (up to 9%) with feldspar and minor biotite and pyroxene crystals. Lithic fragments are mainly lavas which content is variable between 5 and 25%. The most proximal facies, including sand-wave structures and impact sags, produced by ballistic blocks larger than 50 cm, are exposed along the Northern crater wall.

Member B: sequence of prevailing wet surge beds and minor fall deposits. The volume of magma is 0.022 km^3 (D.R.E.) Cohesive, massive to cross-laminated, generally fine ash beds, with abundant accretionary lapilli. In particular the base is a sequence of coarse- to fine-ash surge beds distributed over an area of about 10 km^2, which attains its maximum thickness of 20 cm along the crater walls. Rarely the sequence contains undulated laminae of fine-ash and alignments of coarse ash and thin pumice lapilli fallout beds. Sometimes they are partially eroded and lensoid, due to the surge emplacement. The pumice are variably vesiculated, porphyritic fragments with feldspar, pyroxene and biotite. The top of Member B is a gray to yellow, massive and vesiculated, accretionary lapilli-rich, cohesive fine-ash fallout bed.

Member A: 6 sequences of fall layers each overlain by thin surge beds. The volume of magma is 0.020 km^3 (D.R.E.)

A5 - Juvenile fragments: subaphyric pumices with feldspar, pyroxene and biotite crystals. Lithic fragments: lavas and rare tuffs. Distribution area: ca. 18 km^2.

A4 - Juvenile fragments: variably vesiculated subaphyric pumices with about 2% of feldspar, pyroxene and biotite crystals. Lithic fragments (15%): lava and minor tuffs. In few proximal exposures the fallout deposit contains laminae of surge ash beds. Distribution area: 20 km^2.

A3 - Juvenuile fragments: well vesiculated, often banded, subaphiric pumices similar to those of A2. Lithic fragments: fresh lavas and tuffs. In proximal exposures fine-ash surge lenses are contained in the fallout deposit. Distribution area: 15 km^2.

A2 - Juvenile fragments: variably vesiculated, subaphyric pumices, containing feldspar, pyroxene and biotite crystals. Some fragments have bread-crust surfaces. Lithic fragments: variably altered tuffs and lavas. Thin lenses of laminated surge beds are interbedded in the proximal fallout deposit. Distribution area: 37 km^2.

A1 - Juvenile fragments: pumices similar to those of A0. Lithic fragments: both fresh and hornfelsed lavas and rare tuffs. Distribution area: 23 km^2.

A0 - Juvenile fragments: almost aphyric pumices with less than 1% of feldspar crystals, varying in both vesicularity and color, from light gray to dark gray. Some bombs have bread-crust surfaces. Lithic fragments: mainly tuffs. Distribution area: <1 km^2.

◀ **Fig. 3** Stratigraphic type-section of the Averno 2 Tephra, with indication of the stratigraphic levels sampled for petrographic and geochemical studies in the left side of the section, as short dashes. Pie charts show the results of component analysis performed with SEM at the indicated levels; 1–3 are the types of fragments grouped according to their features (see text for more explanation). Grain-size distribution curves and statistical parameters of selected samples representative of the recognized lithotypes are reported on the right side of the figure

phases that generated Members B and C. The basal fall layer of sub-member A0, dispersed over a narrow area centered on the Torretta locality (Fig. 4a), is mainly composed of pumice lapilli and also includes ballistic blocks and bombs that form impact sags on the underlying paleosol. It is the remnant of a small cone-shaped edifice, SW of the present Averno depression (*I* in Fig. 1b). Dispersal of the fall layer in sub-member A1 (Fig. 4b) suggests that the eruption's vent was likely located in the southwestern concave sector of the present Averno lake depression (*II* in Fig. 1b), next to the earlier Averno 1 eruption vent. Sub-member A2 includes a fall deposit dispersed towards the SW over an area of about 37 km^2 (Fig. 4c). This deposit attains its maximum thickness along both northern and western scarps of the present Averno depression. Both grain-size and thickness of the uppermost surge beds decrease radially from the present lake area. The geometry of impact sags below large ballistic blocks on the underlying ash deposits, indicates a provenance from the present lake. These characteristics, as well as isopachs and isopleths of the fall deposit and distribution of impact sags concur in pointing to the area presently occupied by the lake as the likely vent location. Dispersal of the fall layers in sub-members A3, A4 and A5 (Figs. 4d, e and f) corroborates such a vent location. The fall layer in A4, and the basal portions of sub-members A0 and A2, are the richest in lithic fragments (10–20%) of the whole member. The volume of the variable fall deposits of this member, except for A0 for which there are insufficient thickness data, was calculated using multiple methods (Pyle 1989, 1995; Legros 2000; Dell'Erba 2004—Appendix), and the results are presented in Table 1. The total volume of the fall deposits, calculated using the Dell'Erba (2004), Legros (2000) and Pyle (1989, 1995) methods, is 0.031, 0.020, and 0.028 km^3, respectively. Isopleth reconstruction for the A1–A5 sequence of fall deposits (Fig. 4) indicates that column height (Pyle 1989) varied between 8 and 10 km (Table 1), reaching a maximum during emplacement of A2. The latter was the most widely dispersed fall deposit of the AV2T, and probably represents the climactic phase of the eruption (Table 1). Estimated maximum mass discharge rate (Wilson and Walker 1987) and intensity (Pyle 2000) are 3.2 10^6 kg/s and 9.5, respectively.

The fine fragments within coarse pumice fall deposits (Fig. 3) are mainly (67–80%) highly vesicular particles generated by magmatic fragmentation processes. These deposits also contain subordinate vesicular fragments with pitted surfaces, and rare particles either blocky or with quench cracks of phreatomagmatic origin. In contrast, the ash beds are composed of fragments that are nonvesicular and have quench cracks (66-49%), with most of the vesicular fragments showing pitted surfaces. The described features suggest that these ash beds were mostly generated by phreatomagmatic fragmentation events that affected a vesiculating batch of magma. Lithic fragments generally account for 3–5% of the total components, but in sub-members A0 (10%) and A4 (18%).

Fall deposits of Member A are well sorted, with sorting values always <2, and have unimodal grain-size distributions with modes between -1.5 and -3.0 phi (except for A0, which was sampled in a very proximal exposure and has modal grainsize of -6.0; Fig. 3). The ash layers display bimodal and asymmetric grain-size distributions, with the main mode between 4.5 and 5.0 phi and a secondary one between -2.5 and -3.0 phi (Fig. 3). The bimodality may be due to contemporaneous deposition from pyroclastic surges and fall (Dellino et al. 2004).

Member B This Member is a sequence of cohesive, massive to cross-laminated fine-ash beds containing abundant accretionary lapilli with subordinate thin fall-deposited pumice layers. It is distributed over an area of about 34 km^2, probably by wet-surge currents. The currents flowed preferentially toward the north (Fig. 5b), because remnants of the Archiaverno volcanic edifice formed morphological barriers toward the west and south. The fall layers were dispersed only over a narrow area towards the north.

SEM morphologic analyses (Figs. 3 and 6) indicate that 70% of the juvenile fragments in the ash beds deposited by the wet-surge currents are blocky, often with hydration skin or adhering particles, with a few moderately vesicular fragments affected by quench cracks. Among the juvenile fragments of the fall deposits, highly vesicular, fresh clasts generated by magmatic fragmentation prevail (62–46%). The lithic fragments account only for 10% of the total components, on average. All the ash samples are characterized by well sorted grain-size distributions (1.5–2.0 σ) with a mode at 4.0–4.5 phi. The samples of the fall deposits have a sorting (σ) of 2.0–2.5 and a mode between 3.0 and 0 phi (Fig. 3). The poor sorting and the narrow areal distribution suggest that these deposits were laid down by short-lived, low eruption columns.

Member C This Member is composed of a sequence dominated by dry-surge beds, with minor pumice fall deposits and accretionary lapilli-rich, fine-ash beds. It is dispersed over an area of about 12 km^2, preferentially

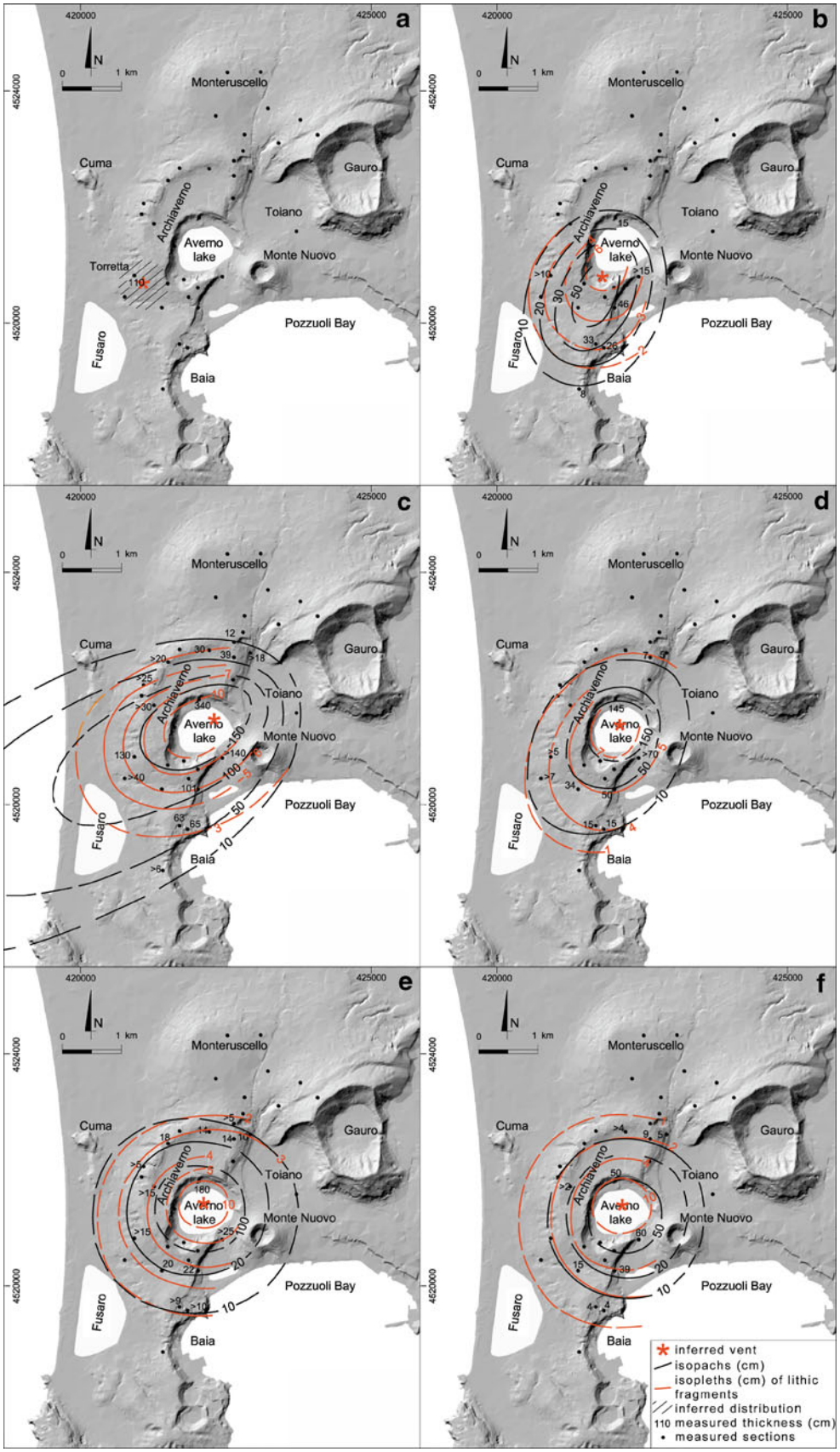

Fig. 4 Isopachs (*in black*) and isopleths (*in red*) distribution of Member A fall deposits

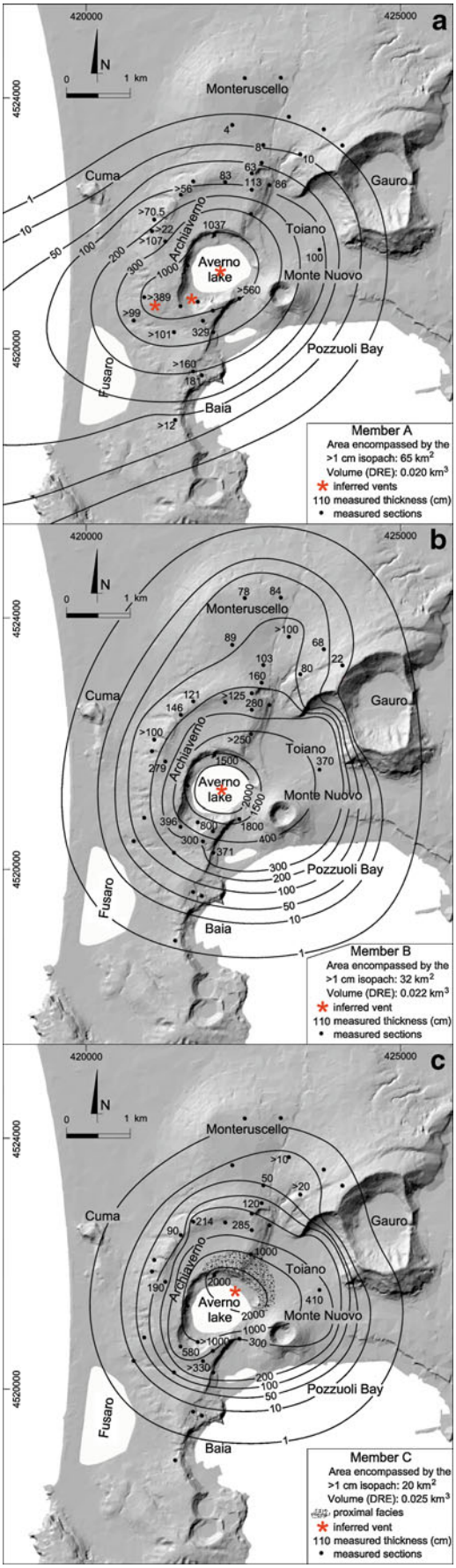

◀ **Fig. 5** Total thickness distribution of Members A, B and C deposits

toward the north, but also drapes the southern portion of the crater wall (Fig. 5c). Proximal deposits, which include sand-wave structures and impact sags produced by ballistic blocks larger than 50 cm, are exposed along the N-NE arched sector of the crater (Figs. 1b and 5c). The sedimentological characteristics of this Member vary significantly with distance; at 1 km from the vent, the pyroclastic sequence is made up of plane-parallel thin laminae of fine- to coarse-ash.

The majority of the juvenile fragments (59–44%) of the coarse- to fine-ash surge deposits show characteristics such as poorly- to non-vesicular blocky morphologies, alteration skins, and minor quench cracks and adhering particles, that suggest a predominantly phreatomagmatic origin. Highly vesicular clasts of magmatic origin only account for 31–46% (Figs. 3 and 6). Lithic fragments content is about 10%. A decrease in the pyroclast vesicularity degree from Member B to Member C is evident in the magmatic particles, which also show thicker bubble walls in Member C. In the pumice fall deposits the juvenile magmatic fragments are more abundant than the phreatomagmatic ones.

Grain-size analyses of the majority of ash samples reveal log-normal distributions with a mode between 1 and 2 phi, and sorting values around 1 (Fig. 3). The good sorting of the samples is probably related to selection due to the traction effect on the particles by diluted and turbulent pyroclastic currents. The samples of the fall deposits have the same grain-size characteristics as those of member B, in particular a poor sorting. This, and the narrow distribution around the vent suggest that these deposits too were sedimented from short-lived eruption columns.

Volumes of erupted magmas of 0.020, 0.022 and 0.025 km^3 (DRE), have been estimated for Members A, B and C, respectively (Figs. 5a, b and c; Table 1; Appendix), corresponding to a total erupted mass of 1.7 10^{11} kg.

Petrography

AV2T includes pumice fragments with variable vesicularity and porphyricity (methods in Appendix): vesicles vary from 45 to 70 vol.%, and phenocrysts from <1 to ~9 vol.%, roughly increasing upsection. Textures vary from aphyric to vitrophyric and glomero-porphyritic, the latter characterized by aggregates of alkali-feldspar and plagioclase. The main paragenetic mineral assemblage comprises predominant phenocrysts of alkali-feldspar, along with phenocrysts and microphenocrysts of biotite, plagioclase, clinopyroxene and magnetite, in order of decreasing abundance, with rare

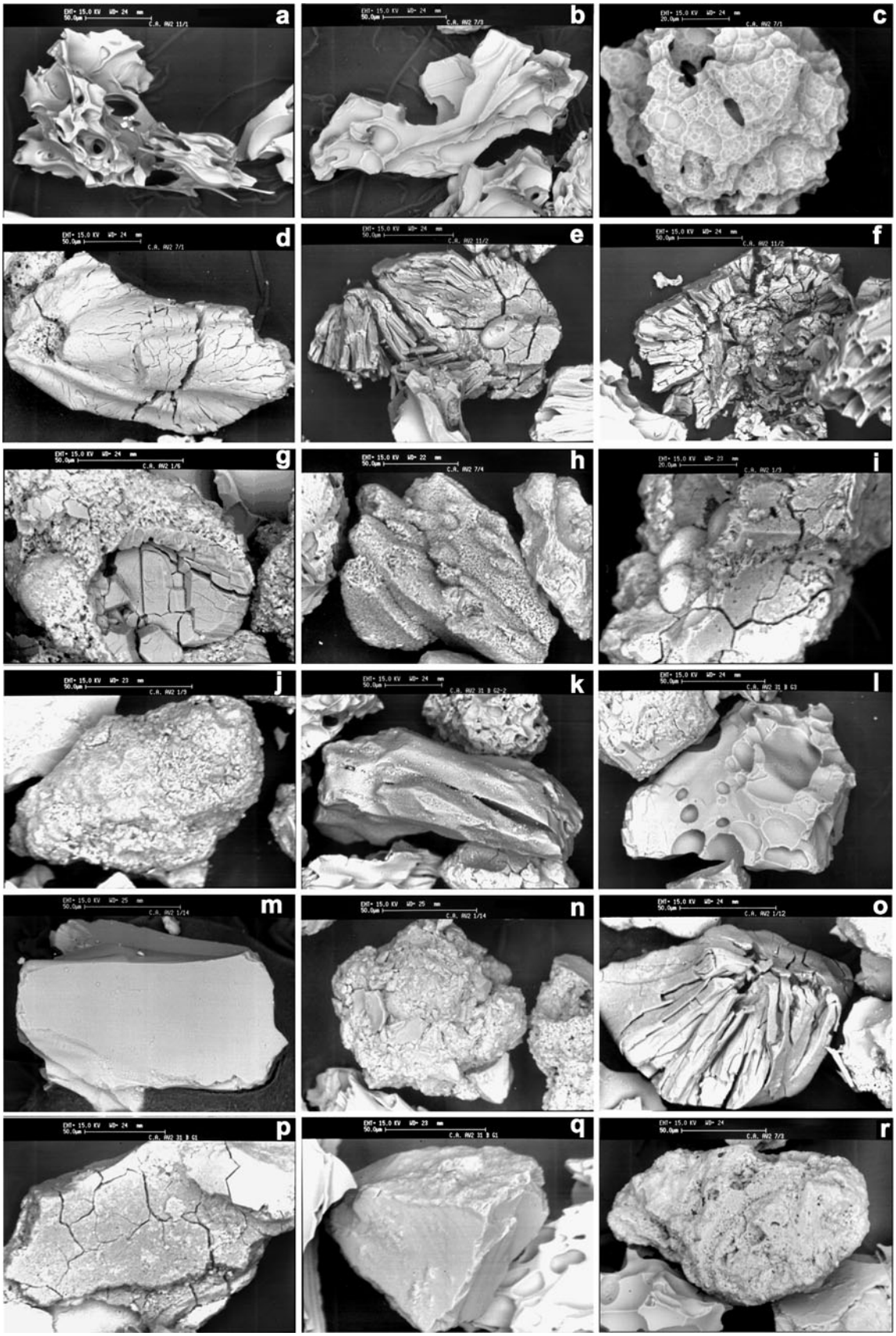
a
b
c
d
e
f
g
h
i
j
k
l
m
n
o
p
q
r

◀ **Fig. 6** SEM imageries of selected pyroclasts of the AV2 deposits. **a-b** angular, highly vesicular fragments with ovoid to elongated vesicles (fall, sub-members A0 and A2, respectively); **c** vesicular fragment with pitted surface (fall, sub-member A1); **d** weakly vesicular fragment with quench cracks (fall, sub-member A1); **e-f** fragments with columnar quench cracks (surge, sub-member A1); **g** fragment with quench cracks and adhering particles (surge, sub-member A1); **h** weakly vesicular fragment with pitting (surge, sub-member A2); **i** nonvesicular clast with quench cracks, pitting and alteration skin (surge, base of Member B); **j** blocky clast with adhering particles and alteration skin (surge, base of Member B); **k** weakly vesicular blocky clast with curviplanar fractures and μ-sized adhering particles (surge, base of Member B); **l** weakly vesicular clast with ovoid vesicles cut by curviplanar fractures (surge, Member B); **m** nonvesicular blocky clast with nearly planar surfaces (surge, Member B); **n** aggregate of μ-sized fresh glass particles (surge, Member B); **o** nonvesicular blocky clast with columnar quench cracks (fall, Member B); **p** nonvesicular clast with quench cracks, curviplanar fractures and hydration skin (surge, Member C); **p** nonvesicular blocky clast with nearly planar surfaces (surge, Member C); **r** lithic fragment (sub-member A2)

sphene and apatite. Alkali-feldspar occurs as the largest phenocrysts, up to 4 mm-long, and shows weak zoning. Plagioclase phenocrysts, rarely exceeding 1.2 mm in size, are commonly strongly zoned (An_{50} to An_{23}; Civetta et al. 1988) and sometimes sieve-textured. Clinopyroxene phenocrysts reach 2.2 mm in size, and display dark green to yellow pleochroism suggesting a high iron content. The clinopyroxene composition varies within the field of salite, according to published data (Civetta et al. 1988). Biotite occurs as up to 1.3 mm phenocrysts. Magnetite and sphene are not larger than 0.5 mm. The complete paragenesis, namely alkali-feldspar, biotite, plagioclase, clinopyroxene and magnetite, is shown only by the most porphyritic samples, i.e. those of Member C. The groundmass is completely glassy; rarely, a few microlites of alkali-feldspar and biotite can be optically resolved. Alteration is common, involving partial transformation of alkali-feldspar and plagioclase phenocrysts to clay minerals, and of biotite phenocrysts to chlorite. Secondary hematite is very common, as acicular crystals and/or thin film within vesicles, while calcite, and glass devitrification only occur in a few fragments.

Geochemistry

The major oxide and trace element contents of the analyzed AV2T samples (methodologies in Appendix) are listed in Table 2. In the Total Alkali-Silica diagram (Le Maitre 1989) most samples classify as trachyte, and a few as phonolite (Fig. 7a). Using the normative nepheline (Ne) versus differentiation index (D.I.) classification grid (Armienti et al. 1983), commonly used for Campi Flegrei rocks (Fig. 7b), samples classify as alkali-trachytes. All samples are silica undersaturated, with normative nepheline ranging from 2.1 to 7.6 wt.% (Table 2 and Fig. 7b), and agpaitic index (A.I.) from 0.88 to 1.01. D.I. and A.I. are positively correlated, with the highest values yielded by the stratigraphically lowermost samples of Member A. Two among the analyzed samples, having A.I. of ~ 1, as well as the highest D.I. values (90.5–90.2) have also small amounts of normative acmite and/or wollastonite, the latter resulting from the high Fe_2O_3/FeO ratio adopted. Thus, these two samples can be further classified as peralkaline alkali-trachytes.

Loss on ignition (L.O.I.) varies from 2.6 to 3.8 wt.%. These values are not unusual for glass and biotite-rich pumice samples from Campi Flegrei eruptions (e.g., D'Antonio et al. 1999; Pappalardo et al. 1999), although

Table 1 Averno 2 eruption parameters

	Volume (pyroclastic deposit) Dell'Erba (2004) method (km^3)	Volume (pyroclastic deposit) Pyle (1989) method (km^3)	Volume (pyroclastic deposit) Legros (2000) method (km^3)	Volume (DRE) Dell'Erba (2004) method (km^3)	Total Erupted Mass (kg)	Magnitude Pyle (2000)	Column height (km)	Mass Discharge Rate (kg/s)	Intensity
AV2-A1 fallout	0.002	0.002	0.002	0.001	$2.4\ 10^9$	2.4	8		
AV2-A2 fallout	0.016	0.010	0.018	0.006	$1.6\ 10^{10}$	3.2	10	$3.2\ 10^6$	9.5
AV2-A3 fallout	0.005	0.002	0.002	0.002	$4.8\ 10^9$	2.7	9		
AV2-A4 fallout	0.005	0.004	0.004	0.002	$4.5\ 10^9$	2.6	9		
AV2-A5 fallout	0.003	0.002	0.002	0.001	$2.6\ 10^9$	2.4	9		
Total	0.031	0.020	0.028	0.012	$2.8\ 10^{10}$				
Member A	0.041			0.020	$4.9\ 10^{10}$	3.7			
Member B	0.045			0.022	$5.4\ 10^{10}$	3.7			
Member C	0.053			0.025	$6.4\ 10^{10}$	3.8			
Total	0.139			0.067	$1.7\ 10^{11}$	4.2			

Table 2 Major oxide (w.%) and trace element contents (ppm), C.I.P.W. Norm, of representative samples of the Averno 2 eruption

Sample	AV2-A0	AV2-A1	AV2-A2 $_{bottom}$	AV2-A2 $_{top}$	AV2-A3	AV2-A4	AV2-A5	AV2-Ba	AV2-Bb	AV2-Ca	AV2-Cb
Section	TO	AM	AM	AM	AM	AM	AM	SC	MR	MR	MR
Member	A	A	A	A	A	A	A	B	B	C	C
Deposit	Fall	Fall	Fall	Fall	Fall	Fall	Fall	Surge	Surge	Surge	Surge
SiO_2	59.79	59.87	60.10	59.59	60.28	58.90	59.29	59.45	58.88	58.82	58.39
TiO_2	0.38	0.41	0.40	0.39	0.41	0.43	0.43	0.43	0.43	0.44	0.45
Al_2O_3	17.59	17.67	17.72	17.59	17.78	17.88	18.20	17.95	18.06	18.20	18.16
Fe_2O_3tot	3.31	3.41	3.37	3.31	3.39	3.54	3.72	3.61	3.75	3.77	3.81
MnO	0.20	0.20	0.20	0.20	0.20	0.16	0.15	0.17	0.15	0.14	0.14
MgO	0.24	0.31	0.26	0.26	0.30	0.44	0.47	0.42	0.49	0.51	0.59
CaO	1.75	1.80	1.75	1.80	1.82	2.11	2.23	2.06	2.27	2.31	2.44
Na_2O	6.15	5.90	5.82	5.94	5.89	5.19	4.76	5.46	4.87	4.82	4.63
K_2O	7.04	6.47	6.93	7.21	6.20	7.92	7.50	7.58	8.13	8.11	8.52
P_2O_5	0.07	0.08	0.06	0.08	0.09	0.12	0.13	0.11	0.11	0.11	0.14
L.O.I.	3.35	3.75	3.26	3.50	3.52	3.16	2.95	2.62	2.70	2.61	2.57
Total	99.87	99.87	99.87	99.87	99.88	99.85	99.83	99.86	99.84	99.84	99.84
Be	31.1	34.2	34.1	34.0	31.9	21.3	17.6	26.2	19.1	18.1	15.8
V	10.1	12.5	11.0	13.2	11.0	30.1	37.6	28.4	40.5	44.0	49.8
Co	1.11	1.65	1.36	1.32	1.34	2.31	2.91	2.24	3.09	3.31	3.74
Zn	111	113	113	107	107	97.4	92.0	98.2	91.4	90.8	89.3
Ga	25.7	27.6	29.0	26.4	24.9	22.6	21.2	24.4	22.7	21.9	20.8
Ge	1.91	1.76	1.86	1.85	1.82	1.57	1.46	1.61	1.47	1.50	1.19
As	76.3	66.1	68.9	63.7	69.3	43.3	35.6	50.1	38.4	34.9	31.7
Rb	530	528	540	529	512	410	397	458	412	401	380
Sr	7.19	14.8	9.86	12.8	13.3	96.9	124	85.2	149	175	218
Y	78.6	70.8	72.6	68.5	70.5	49.9	41.3	52.8	43.7	42.2	37.1
Zr	1,039	1,044	1,021	1,008	1,080	725	596	741	603	561	500
Nb	147	139	137	135	133	91.1	74.4	98.2	78.7	73.7	64.9
Mo	6.04	6.32	6.10	6.18	5.75	6.20	6.11	5.98	6.31	5.98	6.03
Sn	10.8	10.1	10.0	9.85	9.79	7.20	5.88	7.65	5.92	5.83	5.34
Sb	3.10	3.40	3.49	3.19	3.04	2.16	1.65	2.33	1.76	1.69	1.54
Cs	62.4	56.0	55.3	55.8	54.9	38.0	32.3	42.4	33.9	31.7	28.7
Ba	b.d.l.	8.01	b.d.l.	b.d.l.	b.d.l.	38.5	48.9	42.0	66.2	93.1	142
La	185	184	187	180	174	127	104	138	109	104	93
Ce	370	343	348	338	327	235	196	254	207	198	175
Pr	39.6	36.4	35.6	35.9	35.0	26.1	21.8	26.2	22.6	21.3	19.7
Nd	114	120	125	119	111	88	74	90	78	73	68
Sm	18.7	20.7	21.0	20.5	19.2	15.6	12.8	16.5	13.2	12.6	11.6
Eu	1.54	1.36	1.38	1.32	1.24	1.71	1.80	1.67	1.91	1.87	1.97
Gd	16.3	15.1	14.1	14.5	14.3	11.3	9.13	11.1	9.61	8.98	8.17
Tb	2.25	2.32	2.30	2.16	2.12	1.62	1.38	1.76	1.49	1.39	1.30
Dy	11.9	12.9	12.2	12.1	12.3	8.90	7.93	9.26	7.81	6.96	6.56
Ho	2.54	2.41	2.32	2.39	2.36	1.69	1.39	1.78	1.49	1.38	1.39
Er	7.37	6.43	6.36	6.81	6.75	4.81	4.22	4.95	3.96	3.79	3.34
Tm	1.09	1.16	1.04	1.05	1.03	0.77	0.59	0.80	0.68	0.58	0.55
Yb	7.07	7.65	7.73	7.27	7.39	5.15	4.20	5.46	4.27	4.18	3.65
Lu	1.26	1.24	1.23	1.23	1.23	0.83	0.70	0.88	0.72	0.70	0.64
Hf	24.5	23.8	24.1	23.1	22.5	16.1	12.5	16.7	13.3	12.8	11.1
Ta	9.01	8.90	8.78	8.67	8.56	6.11	4.95	6.63	5.16	4.84	4.40
W	9.15	9.79	9.80	9.87	9.67	9.09	8.82	9.09	8.82	8.68	8.60
Pb	81.2	79.2	78.7	80.2	77.4	67.4	64.9	72.3	66.2	63.0	61.6
Bi	0.76	0.65	0.62	0.60	0.66	0.48	0.40	0.53	0.43	0.39	0.37
Th	109	108	107	106	101	70.7	56.5	78.2	59.3	54.7	49.0
U	31.9	34.4	33.6	33.7	31.9	22.5	17.8	24.8	18.6	17.0	15.2

Table 2 (continued)

Sample	AV2-A0	AV2-A1	AV2-A2 $_{bottom}$	AV2-A2 $_{top}$	AV2-A3	AV2-A4	AV2-A5	AV2-Ba	AV2-Bb	AV2-Ca	AV2-Cb
Section	TO	AM	AM	AM	AM	AM	AM	SC	MR	MR	MR
Member	A	A	A	A	A	A	A	B	B	C	C
Deposit	Fall	Fall	Fall	Fall	Fall	Fall	Fall	Surge	Surge	Surge	Surge
C.I.P.W. norm											
Or	43.10	39.78	42.39	44.21	38.02	48.40	45.75	46.06	49.46	49.29	51.76
Ab	39.15	44.99	42.05	38.64	47.92	32.09	36.91	35.02	30.38	30.27	26.25
An	0.00	2.73	1.82	0.04	3.91	2.17	6.34	2.14	3.51	4.19	3.71
Ne	7.57	3.76	4.83	7.32	2.06	7.22	2.52	6.77	6.52	6.32	7.60
Ac	0.69	0.00	0.00	0.00	0.00	0.00	0.00	0.00	0.00	0.00	0.00
Di	6.90	5.18	5.84	6.62	4.18	6.69	3.58	6.52	6.25	5.83	6.60
Wo	0.23	0.00	0.00	0.43	0.00	0.00	0.00	0.00	0.00	0.00	0.00
Ol	0.00	0.72	0.33	0.00	1.07	0.40	1.75	0.46	0.78	0.96	0.85
Mt	1.20	1.60	1.57	1.55	1.58	1.65	1.73	1.67	1.74	1.74	1.76
Il	0.75	0.81	0.79	0.77	0.81	0.84	0.84	0.84	0.84	0.86	0.88
Ap	0.17	0.20	0.15	0.20	0.22	0.29	0.32	0.27	0.27	0.27	0.34
Total	99.77	99.76	99.77	99.77	99.76	99.76	99.74	99.75	99.74	99.74	99.74
D.I.	90.51	88.53	89.27	90.17	88.00	87.71	85.18	87.85	86.36	85.88	85.60
A.I.	1.01	0.95	0.96	1.00	0.92	0.96	0.88	0.96	0.93	0.92	0.93

C.I.P.W. norm calculated with $Fe_2O_3/FeO=0.5$ for trachytic rocks (Middlemost 1989). Key for Section: TO: La Torretta; AM: Cava dell'Amministratore; SC: La Sciarrera; MR: Monte Russo; D.I. (Thornton and Tuttle 1960): normative Or + Ab + Ne + Ac; A.I. (agpaitic index): Na_2O (mol.%) + K_2O (mol.%)/Al_2O_3 (mol.%); b.d.l.: below detection limit; n.a. = not analyzed

they could partially result from low-temperature alteration. However, altered fragments were carefully avoided during sample preparation for chemical and isotopic analyses (see Appendix). The whole range of D.I. values is between 90.5 and 85.2.

Variation diagrams of selected major oxide and trace element contents vs. CaO wt.% as a differentiation index (Fig. 8), show regular, nearly linear variations. In detail, SiO_2 and Na_2O increase, whereas K_2O, TiO_2, MgO, Al_2O_3, Fe_2O_3tot, and P_2O_5 (Table 2) decrease with decreasing CaO. These variations, although small, can be explained at first blush by fractionation of dominant alkali-feldspar and minor Fe-rich clinopyroxene, biotite, plagioclase and Ti-magnetite, as observed in thin section. The variation in trace element concentrations is large with respect to that of major oxides. Vanadium (from ca. 50 to 10 ppm) and cobalt (from ca. 3.7 to 1.1 ppm) decrease with progressive magma evolution, behaving compatibly, probably fractionated by ferro-magnesian minerals; strontium also behaves as a compatible element, decreasing from more than 200 ppm to less than 10 ppm, being incorporated by alkali feldspar. All other trace elements (e.g., Rb, Cs, Ba, Y, Zr, Nb, REE except Eu, Hf, Ta, Pb, Th and U) increase, generally by a factor of two, from less- to more-evolved rocks (Fig. 8; Table 2), thus showing incompatible behavior. Chondrite-normalized REE patterns (not shown) are parallel for all the analyzed samples, suggesting that their variation is strongly controlled by the degree of chemical evolution of magmas. All patterns display significant fractionation for light and intermediate, with respect to heavy, REE elements, and a strong negative Eu anomaly that deepens from less to more evolved samples (Eu/Eu*=0.59-0.22), testifying to a possible role for alkali-feldspar during magma evolution.

Relevant geochemical parameters are plotted against the stratigraphic position of the analyzed samples in the chemostratigraphy of Fig. 9. From the figure, it is evident that the first erupted, peralkaline alkali-trachytic magma is more evolved, and that the degree of chemical evolution decreases upwards.

The $^{87}Sr/^{86}Sr$ ratios of whole rock and separated glass, feldspars and clinopyroxenes (Table 3), vary from ca. 0.70749 to ca. 0.70754 from base to top of the AV2T pyroclastic sequence (Figs. 8 and 9). Generally at the base of the sequence the Sr isotopic composition of the feldspars is slightly less radiogenic than that of the glass. The isotopic data were processed with Isoplot 3.00 software (by K.R. Ludwig, http://bgc.org/isoplot_etc/software.html), in order to individuate different modes, representing distinct isotopic compositions. Analysis of the Sr isotopes frequency histogram (Fig. 10) shows two modes. One mode ($^{87}Sr/^{86}Sr$= 0.707507) mostly includes the first erupted, more evolved and less radiogenic magma represented in the lower portion of Member A. The second mode ($^{87}Sr/^{86}Sr$=0.707531) is defined by the later erupted, less evolved and more radiogenic magma that produced the upper portion of the stratigraphic sequence (Fig. 9). In contrast $^{143}Nd/^{144}Nd$ ratios are similar within analytical error (Table 3), around an average value of ≈0.512458. Figure 10 also shows

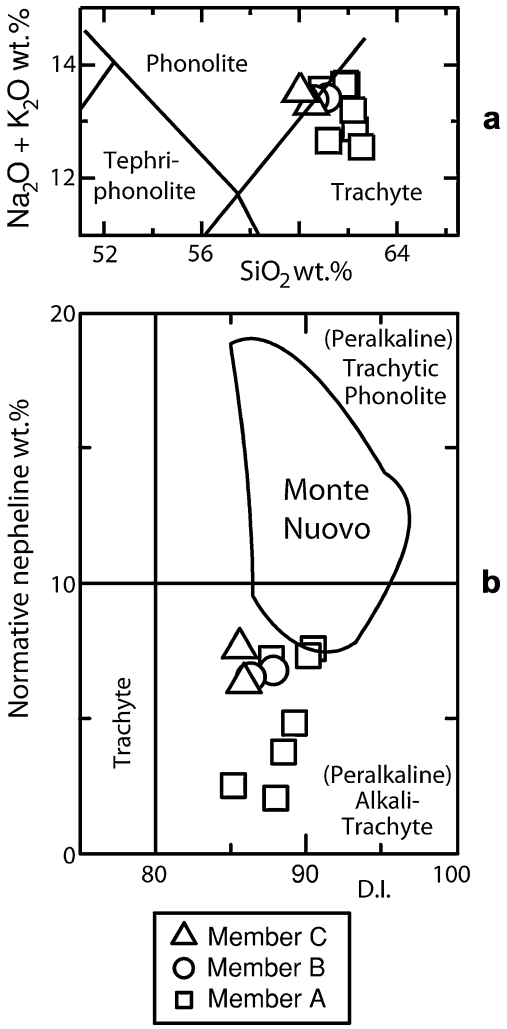

Fig. 7 **a** T.A.S. (Le Maitre 1989) and **b** normative Ne-D.I. (Armienti et al. 1983) classification diagrams for Averno 2 products. The data field for the Monte Nuovo eruption products is based on data from Armienti et al. (1983), Di Girolamo et al. (1984), Rosi and Sbrana (1987), Ghiara (1989-90), D'Oriano et al. (2005) and Piochi et al. (2005)

frequency histograms for abundance of selected trace elements, revealing two extreme modes, that represent the first- and last-erupted magma compositions.

Discussion

History of the Averno 2 eruption

The presented structural, stratigraphical and sedimentological data (Figs. 2 and 3) suggest that the eruption was characterized by three explosive phases, with variable dynamics and dispersal of the pyroclastic products.

The first phase of the eruption began with dominant magmatic and minor phreatomagmatic explosions from a vent located SW of the present Averno lake (*I* in Fig. 1b). These explosions generated a very low eruption column, and then turbulent pyroclastic density currents, that together formed the fall and surge deposits of the A0 sequence of Member A (Fig. 4a). The eruption continued from a new vent opened in the southwestern concave sector of the Averno lake depression (*II* in Fig. 1b) with generation of an 8 km high eruption column, fed mainly by magmatic explosions, that laid down the A1 sequence, composed of a fall deposit (Fig. 4b) overlain by minor surge beds. At this stage the vent further shifted toward the center of the present lake (*III* in Fig. 1b) and the eruption reached its climax, producing an oscillating eruption column that reached the maximum height of 10 km, with a mass discharge rate of $3.2*10^6$ kg/s. Contemporaneous to this magmatic column, sporadic phreatomagmatic explosions also took place, probably through an unlocated but nearby secondary vent. This explosive activity produced the A2 sequence, the most widely distributed of the AV2T (Fig. 4c), including a fall deposit overlain by, and interbedded with minor surge beds. The eruption continued in the central part of the present lake depression with magmatic and a few phreatomagmatic explosions, generating an eruption column that reached a maximum height of about 9 km. This activity generated the subsequent A3, A4 and A5 sequences, composed of dominant fall deposits (Figs. 4d, e, f) with minor surge beds. During emplacement of the A4 sequence, fractures appear to have opened, as suggested by the increase in lithics content, allowing ground- and/or sea-water to enter the shallow feeding system. This change in structural conditions produced a change in eruption dynamics and triggered onset of the second phase of the Averno 2 eruption. This phase was dominated by explosions driven by a very efficient water-magma interaction, with only a few episodes of magmatic explosivity, which generated low, short-lived eruption columns during the later stages of the activity. This second phase deposited Member B, a sequence dominated by wet-surge beds, with minor fall deposits, dispersed preferentially northward from a vent still located in the center of the present lake (Fig. 5b). The pre-existing Archiaverno tuff ring acted as a geomorphic barrier to the surge currents. Another change in vent location and eruption characteristics marked the onset of the third phase of the eruption, which generated Member C. The eruption vent shifted towards the N-NE arched sector of the Averno lake depression (*IV* in Fig. 1b; Fig. 5c), as suggested by distribution of the proximal facies of the pyroclastic deposits, distribution and geometry of impact sags by ballistic blocks and bombs, and Member C deposits draping the southern crater walls. This activity was dominated by phreatomagmatic explosions generated by efficient water-magma interaction, alternate with episodic magmatic explosions.

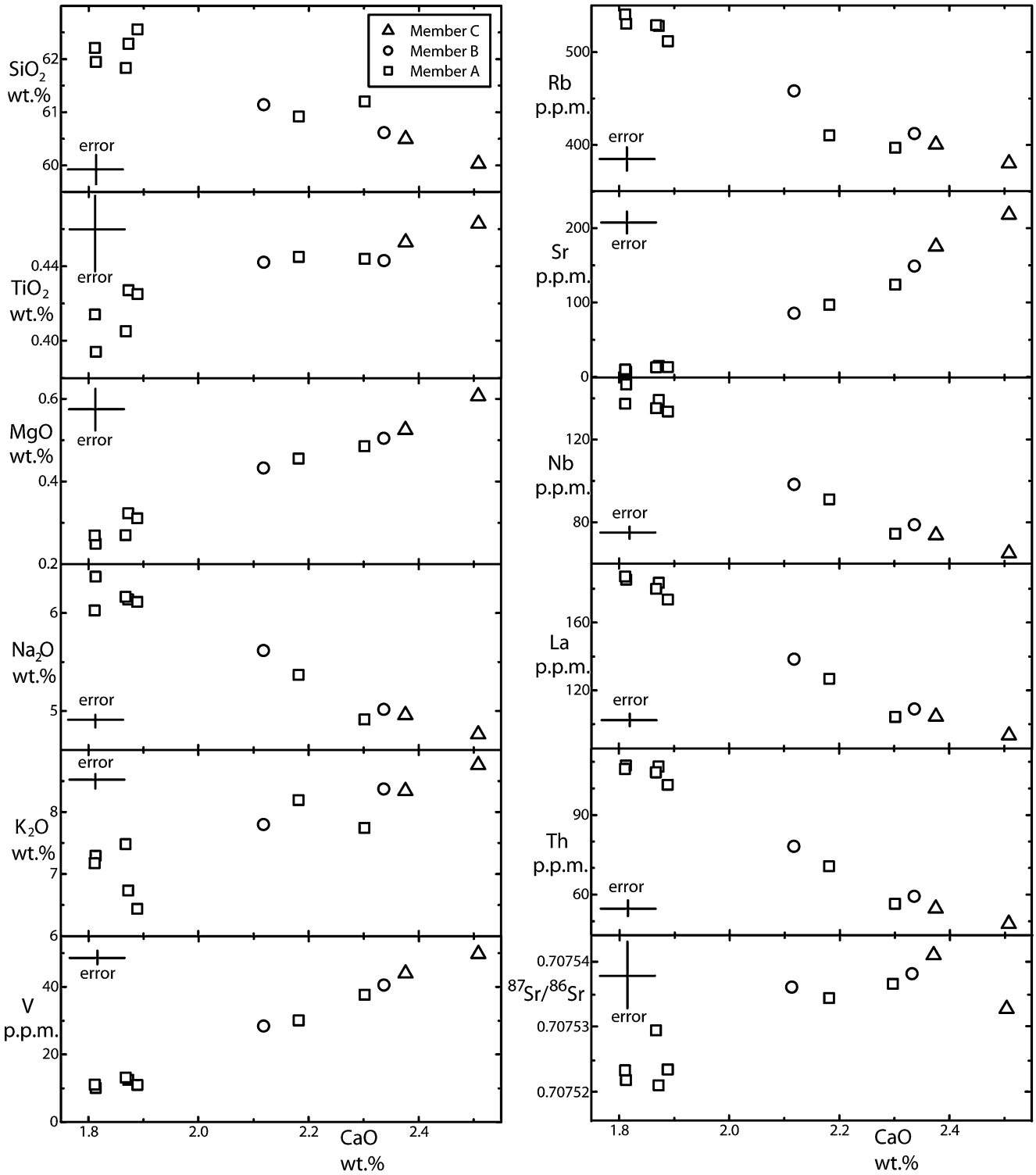

Fig. 8 Variation diagrams of selected major oxide, trace element contents and $^{87}Sr/^{86}Sr$ versus CaO wt.% as differentiation index. Data from Tables 2 and 3

In summary, Member A was produced by three vents progressively active from SW toward the center of the present lake. During emplacement of this Member the eruption, dominated by magmatic explosions, reached its climax (sub-member A2), although the total erupted volume (0.020 km^3—DRE) was only about 1/3 of the AV2T. The eruption phases which produced Members B and C were dominated by phreatomagmatic explosions

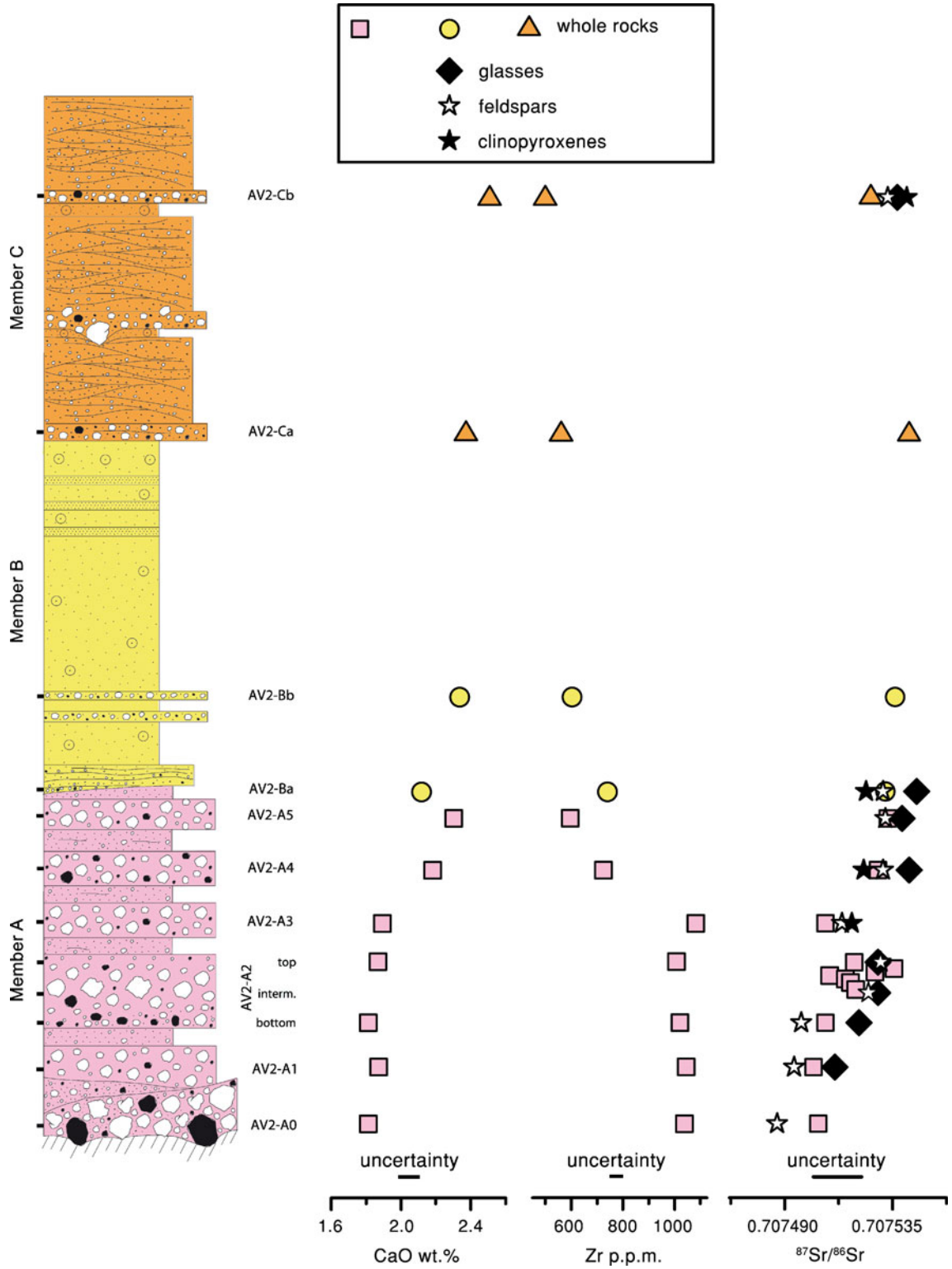

Fig. 9 Chemostratigraphy of the products of the Averno 2 eruption. Data from Tables 2 and 3

generating variably distributed pyroclastic surges from vents progressively shifting toward NE. These explosions were fed by more and more crystallized and degassed magma, which accounted for the remaining 2/3 of the total volume (Member B: 0.022 km^3; Member C: 0.025 km^3—DRE).

Magmatic processes

Notwithstanding the small volume of erupted magma (ca. 0.07 km^3 DRE), the products of this eruption show a slight variability of mineralogical, geochemical and Sr-isotopic

Table 3 Sr and Nd isotope compositions of selected whole rocks, glasses and mineral phases from the Averno 2 erupted products

Sample	$^{87}Sr/^{86}Sr$ w.r.	2σ	$^{143}Nd/^{144}Nd$ w.r.	2σ	$^{87}Sr/^{86}Sr$ glass	2σ	$^{87}Sr/^{86}Sr$ feld.	2σ	$^{87}Sr/^{86}Sr$ cpx	2σ
AV2-A0	0.707504	0.000007	0.512456	0.000007	n.a.		0.707487	0.000007	n.a.	
AV2-A1	0.707502	0.000006	0.512461	0.000006	0.707511	0.000006	0.707494	0.000006	n.a.	
AV2-A2 bottom	0.707507	0.000005	0.512460	0.000005	0.707521	0.000006	0.707497	0.000007	n.a.	
AV2-A2 intermediate	n.a.		n.a.		0.707529	0.000006	0.707525	0.000007	n.a.	
AV-24	0.707521	0.000006								
AV-25	0.707519	0.000006								
AV-26	0.707518	0.000006								
AV-27	0.707513	0.000008								
AV-28	0.707528	0.000006								
AV-29	0.707534	0.000005								
AV2-A2 top	0.707519	0.000005	0.512467	0.000006	0.707529	0.000006	0.707530	0.000007	n.a.	
AV2-A3	0.707507	0.000006	0.512461	0.000006	n.a.		0.707514	0.000007	0.707518	0.000006
AV2-A4	0.707529	0.000008	0.512458	0.000005	0.707542	0.000006	0.707531	0.000007	n.a.	
AV2-A5	0.707533	0.000007	n.a.		0.707539	0.000006	0.707532	0.000006	n.a.	
AV2-Ba	0.707532	0.000007	n.a.		0.707545	0.000006	0.707531	0.000007	0.707524	0.000008
AV2-Bb	0.707536	0.000006	0.512459	0.000005	n.a.		n.a.		n.a.	
AV2-Ca	0.707542	0.000008	0.512458	0.000004	n.a.		n.a.		n.a.	
AV2-Cb	0.707526	0.000008	0.512465	0.000004	0.707537	0.000007	0.707533	0.000007	0.707541	0.000007

Sr– and Nd–isotope data are reported to the accepted values of $^{87}Sr/^{86}Sr=0.71025$ for NIST–SRM 987 and of $^{143}Nd/^{144}Nd=0.51185$ for La Jolla

n.a. not analyzed

characteristics, that sheds light on pre- and syn-eruption magmatic processes. The small range of composition, and the detected co-variations of major oxide and trace element concentrations, shown by the Averno 2 products (CaO from 2.4 to 1.8 wt.%), could result from a fractional crystallization process of a silica-rich magma, involving the mineral phases present in the rocks. This process is suggested by regular variation of major oxide and trace element contents with CaO as differentiation index (Table 2 and Fig. 8), as well as by linear relationships between pairs of incompatible trace

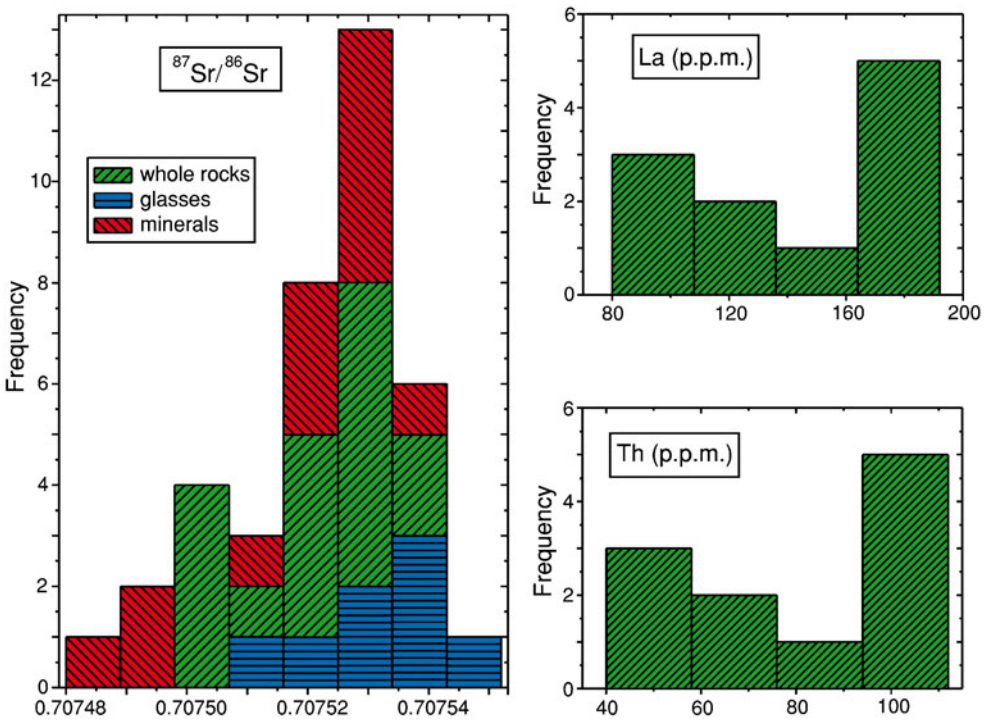

Fig. 10 Frequency histogram of $^{87}Sr/^{86}Sr$ measured in whole rocks, glasses and minerals (feldspar and clinopyroxene) of representative Averno 2 Tephra samples. Data from Table 3. Frequency histograms of La and Th contents measured in AV2T whole rocks. Data from Table 2

elements, with regression lines passing through zero (not shown), and geochemical modeling results (Table 4).

Sr-isotopic variations, however, indicate that open-system processes, such as crustal contamination or magma mingling/mixing, operated in the magmatic system, rather than simple fractional crystallization. Crustal contamination can be confidently ruled out, as it does not explain the detected $^{87}Sr/^{86}Sr$ vs. Sr variation (Fig. 11c). In fact, such a process would increase the $^{87}Sr/^{86}Sr$ value as a function of degree of chemical evolution. Instead binary mingling/mixing between two magmas differing both in degree of chemical evolution and in $^{87}Sr/^{86}Sr$, better explain both geochemical and isotopic data. Generally, mineralogical and isotopical disequilibria are strong evidence for such a process. However, the first erupted AV2 magma was nearly aphyric (see Petrography), thus no crystals from it could be identified in the products of the eruption. Furthermore, the difference between the $^{87}Sr/^{86}Sr$ of the two magmas is very small, though beyond the analytical uncertainty (Fig. 9).

Detailed geochemical and isotopic studies have highlighted that mingling/mixing is the main open-system magmatic process at Campi Flegrei (Orsi et al. 1995; Civetta et al. 1997; D'Antonio et al. 1999; de Vita at al. 1999; Morgan et al., 2004; Tonarini et al. 2009; Arienzo et al. 2009, 2010; Di Renzo et al. 2010). Therefore, in order to explain all the detected geochemical and isotopical variations, we propose that two isotopically distinct magma batches were involved in the Averno 2 eruption. The chemostratigraphy shows that the first-erupted magma (samples AV2-A0 and A1, base of Member A in Fig. 9) is the most evolved, least radiogenic batch ($^{87}Sr/^{86}Sr$ ca. 0.70751). The products of Members B and C are slightly less evolved and homogeneous (CaO from 2.2 to 2.4 wt.%), and more enriched in radiogenic Sr ($^{87}Sr/^{86}Sr$ ca. 0.70754; Fig. 9). Consequently, they represent the most radiogenic magma batch. These two end-members mingled/mixed before and/or during extrusion of Member A. In fact, this member is slightly chemically zoned and characterized by the widest range of both chemical and Sr-isotopic composition of the whole sequence. The samples of sub-member A2 are intermediate in isotopic composition between the two isotopically distinct end-members, testifying to continuation of the mixing process. Mixing is also indicated by the occurrence of two distinct modes, representing the two magmas, in trace element and $^{87}Sr/^{86}Sr$ histograms (Fig. 10). We tested the mixing hypothesis using the Langmuir et al. (1978) binary equation applied to $^{87}Sr/^{86}Sr$, as well as to CaO, Sr and La contents, as representative of the composition of all the analyzed whole-rock samples. We assigned the most and least radiogenic Sr-enriched AV2T samples, having the highest and lowest incompatible trace element contents, as end-members. The mixing curves

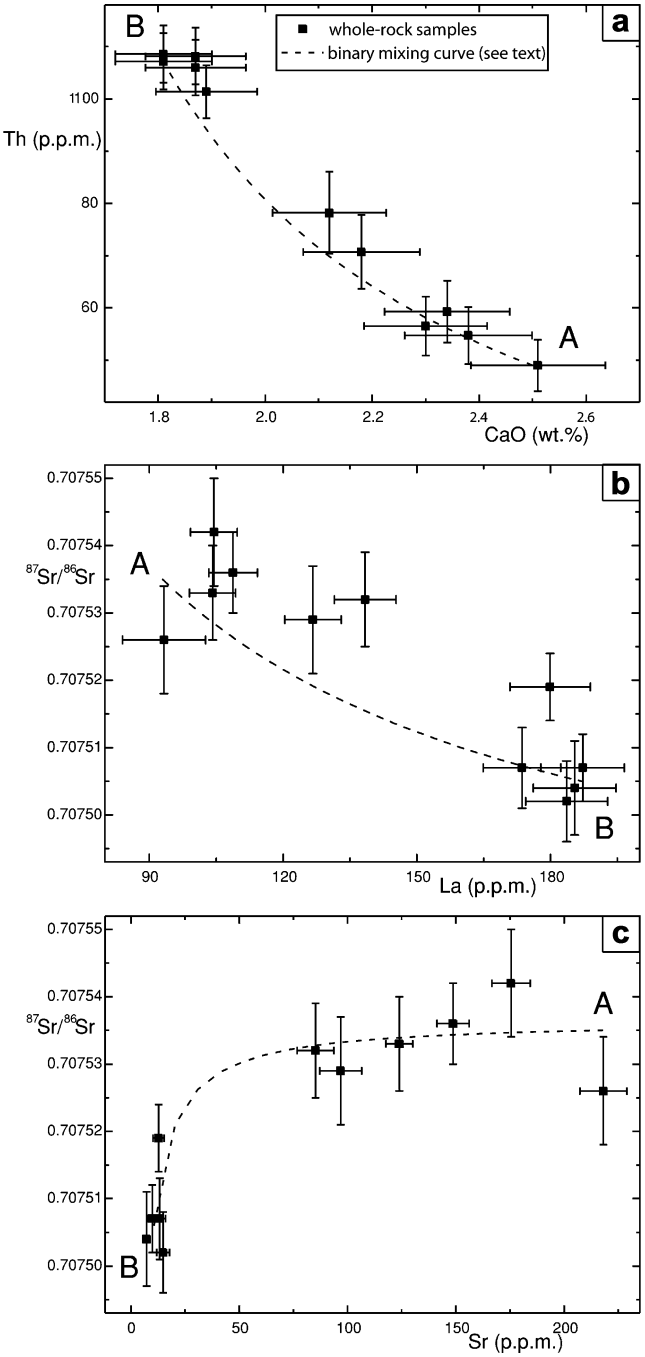

Fig. 11 Variation diagrams of CaO, selected trace elements and Sr-isotopic ratio data for Averno 2 Tephra samples. Data from Tables 2 and 3. The dashed curves indicate the result of binary mixing modeling calculated through the Langmuir et al. (1978) equation. A and B represent the end-members which compositions are: A: CaO= 2.5 wt.%, Th=49 p.p.m., La=93 p.p.m., Sr=218 p.p.m., $^{87}Sr/^{86}Sr$= 0.707535; B: CaO=1.8 wt.%, Th=109 p.p.m., La=187 p.p.m., Sr= 10 p.p.m., $^{87}Sr/^{86}Sr$=0.707505

calculated for Th vs. CaO content, and for Sr-isotopic ratio vs. Sr and La contents match well the whole-rock data (Fig. 11). The good match between measured and calculated data is good evidence that for AV2T, as well as for the

majority of Campi Flegrei magmas, major oxide and trace element variations cannot be used to unequivocally discriminate between open and closed system processes. For this reason isotopic analysis, particularly of Sr, has become a more and more important tool to discriminate between closed-system fractional crystallization and open-system magma mingling/mixing in the Campi Flegrei magmatic system (e.g., Orsi et al. 1995; Civetta et al. 1997; D'Antonio et al. 1999; 2007; de Vita at al. 1999; Pappalardo et al. 2002b; Tonarini et al. 2004, 2009; Arienzo et al. 2009; 2010; Di Renzo et al. 2010).

During the Averno 2 eruption, an overall vent migration from SW to NE occurred along a fault system bordering the La Starza block toward the NW (Fig. 1b). This structural lineament is still active, as indicated by ground deformation during the recent bradyseismic events (Orsi et al. 1999a). The four recognized vents opened at the intersection of this fault system and NW-SE trending faults of the conjugated system of the La Starza resurgent block (Orsi et al. 1996). On the basis of total distance of vent migration, it is possible to estimate that the feeding fissure was about 2 km long. Vent migration and the small volume of emitted magma (0.07 km^3 DRE) suggest that the eruption was fed from a dyke-like reservoir, 2 km long, and probably tens of meters wide and hundreds of meters thick, trapped within the NE-SW fault system.

In Fig. 12 a possible reconstruction of the main eruption phases, and magma withdrawal dynamics during the eruption is schematized. Before onset of the eruption, the reservoir was filled only with the peralkaline and less radiogenic magma A. Uprise of magma B (Fig. 12), less evolved and thus probably hotter and more enriched in radiogenic Sr, could have triggered the eruption (e.g. Murphy et al. 2000). The first phase extruded this magma through vent *I* (Fig. 12). Magma mixing is commonly accepted as a triggering mechanism for explosive eruptions of felsic magmas (Sparks et al. 1977; Folch and Martì 1998; Murphy et al. 1998; Boudon et al. 2008, and references therein). Similar processes have been recently envisaged for the Astroni and Agnano-Monte Spina eruptions, in the northeastern sector of the Campi Flegrei caldera, and for the Campanian Ignimbrite (Civetta et al. 1997; de Vita et al.

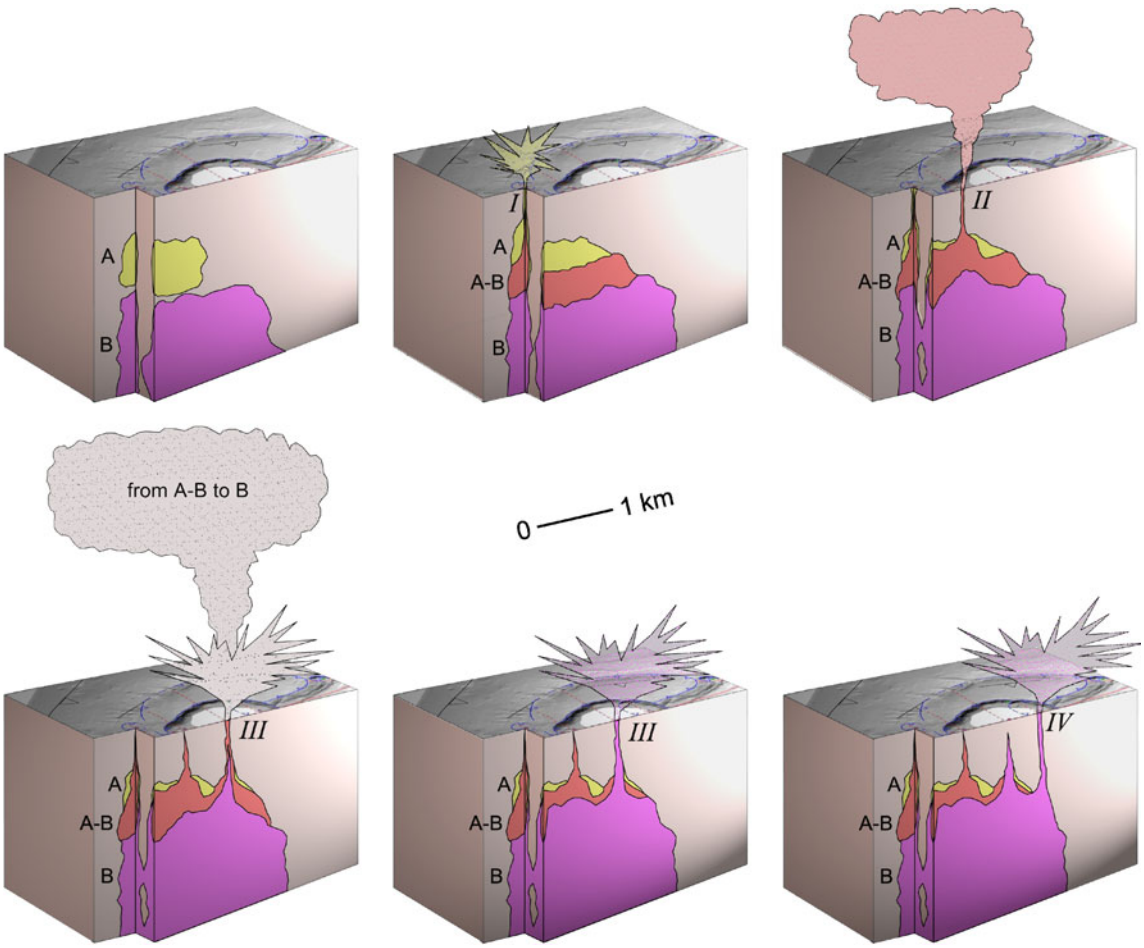

Fig. 12 Cartoon of the withdrawal and eruption history of the Averno 2 main eruption phases. The vent positions (from *I* to *IV*) are reported on the simplified cross section. A = peralkaline alkali-trachytic less radiogenic magma; B = alkali-trachytic more radiogenic magma

1999; Tonarini et al. 2009; Arienzo et al. 2009; 2010). Furthermore, Perugini et al. (2010) have estimated that mixing began 9 days prior to the Averno 2 eruption. The vent then migrated northeastward (vent *II*), although the eruption was still fed mostly by magma A. Soon afterward, the eruption vent migrated closer to the center of the present lake (vent *III*). During this phase, fed by A and A-B mixed magmas, the eruption reached its climax, probably favored by the involvement of the least evolved and hotter magma B, which was probably also richer in gas, since it was more crystalline than magma A. From then until its end, the eruption was fed only by magma B (Fig. 12).

It is interesting to note that the $^{87}Sr/^{86}Sr$ and $^{143}Nd/^{144}Nd$ values of the first-erupted Averno 2 and the last-erupted NYT magmas are similar ($^{87}Sr/^{86}Sr$~0.70750, $^{143}Nd/^{144}Nd$~0.51246) (Orsi et al. 1995; D'Antonio et al. 2007; Di Renzo et al. 2010), although differently evolved. Such a similarity suggests the hypothesis that the Averno 2 eruption could have been fed by a magma derived by differentiation of residual NYT magma. This hypothesis can be tested by geochemical modeling using an average NYT trachyte (Orsi et al. 1995) as parent magma. The results of the modeling performed with major oxides (Table 5) show that the Averno 2 peralkaline alkali-trachyte (AV2-A0) can be derived from the NYT trachyte by crystallizing about 82% of an assemblage constituting 63% sanidine, 17.6% plagioclase, 10.2% salite, 6.0% Ti-magnetite, 2.3% biotite and 1.0% apatite (sum of the squares of residuals is 0.03). The Rayleigh fractionation modeling also gives good matches between measured and calculated concentrations of trace elements in the daughter magma.

Overall, the geochemical and isotopic data, as well as the results of geochemical modeling, suggest that a small pocket of magma left after the NYT eruption may have differentiated at shallow depth to provide a slightly peralkaline, alkali-trachytic magma. This magma was then intercepted by a less evolved magma, more enriched in radiogenic Sr and of deep provenance, that first mixed with the residual magma (Member A), and later dominated the eruption during the phases that generated Members B and C (Fig. 12).

Conclusions

The results of our investigations stress that a detailed reconstruction of the sedimentological and stratigraphic characteristics of the depositional sequence, the structural evolution and setting of the vent area, and the architecture of the magmatic feeding system, is needed to underpin interpretations of the relationships among structural pattern, vent location, eruption dynamics, magma composition, and withdrawal dynamics of an eruption. Knowledge of such relationships for an active volcano, is fundamental in long- and short-term volcanic hazards assessment, as well as in eruption forecasting. This knowledge becomes essential for volcanoes located in densely populated areas, such as the Neapolitan one, where the very high value exposed to potential volcanic hazards induces a very high volcanic risk (Orsi et al. 2003).

The AV2 eruption, one of the youngest from Campi Flegrei caldera, took place in its western sector and was fed by a small-volume (ca. 0.07 km^3 DRE), alkali-trachytic magma. It was a purely explosive event, with phreatomagmatic fragmentation processes dominating over magmatic ones, and characterized by vent migration. The feeding magma resulted from mingling/mixing of two compositionally distinct end-members, shortly predating and/or accompanying the event. Mingling/mixing, with consequent destabilization of the feeding system, probably triggered the eruption as has been the case for most of the Phlegraean events (e.g., Arienzo et al. 2010, and references therein). Vent migration occurred along a 2 km-long fissure, part of a NE-SW fault system frequently re-activated in relation to volcanic activity and caldera resurgence, and still active as shown by the monitored ground deformation during the recent unrest episodes (Orsi et al. 1999a). The AV2 eruption provides evidence of the intimate interplay among structural setting, magmatic processes, and eruption and withdrawal dynamics, even in a low-magnitude event.

The AV2 eruption, together with that of Monte Nuovo, has been considered as the type event for a low-magnitude eruption, the most likely (60% probability) explosive event to occur, in case of renewal of volcanism at Campi Flegrei in short- to mid-term (Orsi et al. 2009). Its evolution emphasizes that involvement of an active fault system can fundamentally influence the eruption vent/vent area and thereby the eruption's impact on the territory. In particular vent migration over several kilometers can significantly extend the areas exposed to variable potential volcanic hazards.

Acknowledgements Carandente A. and Belviso P. are warmly thanked for the great support in samples preparation and analytical work perfomed at Istituto Nazionale di Geofisica e Vulcanologia—Osservatorio Vesuviano. F. Dell'Erba and Isaia R. are thanked for the kind help in stratimetric data collection and processing. D. Palladino, B. Villemant and R. Cioni are thanked for very useful revision, comments and suggestions.

This work has been financially supported by the Italian Departement for Civil Defence in the framework of the INGV-DPC 2005-2007 V3 and 2009-2010 UNREST projects.

Appendix: methodologies

The results on the Averno 2 Tephra (AV2T) presented and discussed in this paper were collected through the application of various methods.

Table 4 Results of geochemical modeling (Stormer and Nicholls 1978) for the transition from alkali-trachyte to peralkaline alkali-trachyte of Averno 2

Major oxides (wt.%)					
Sample	AV2-Cb	AV2-A0			
	Parent magma	Daughter magma	Difference between parent and daughter magmas		
	measured	measured	observed	calculated	observed-calculated (residuals)
SiO_2	60.03	61.95	1.93	1.82	0.102
TiO_2	0.46	0.39	-0.70	-0.08	0.006
Al_2O_3	18.67	18.22	-0.45	-0.47	0.021
Fe_2O_3tot	3.92	3.43	-0.49	-0.54	0.047
MnO	0.14	0.21	0.07	0.09	-0.016
MgO	0.61	0.25	-0.36	-0.42	0.060
CaO	2.51	1.81	-0.70	-0.61	-0.086
Na_2O	4.76	6.37	1.61	1.80	-0.185
K_2O	8.76	7.29	-1.47	-1.30	-0.166
P_2O_5	0.14	0.07	-0.07	-0.29	0.216
Total	100.00	100.00			
Sum of the squares of residuals					0.133
Subtracted minerals		Amounts relative to initial magma	Absolute amounts		
Sanidine (Or_{72})		38.42	76.99		
Plagioclase (An_{40})		4.85	9.73		
Clinopyroxene ($Wo_{47}Fs_{22}En_{31}$)		2.11	4.23		
Biotite		1.85	3.70		
Ti-magnetite (Usp_{24})		1.91	3.83		
Apatite		0.76	1.52		
Total relative to initial magma		49.90	100.00		
Trace elements (p.p.m.)					
Sample	AV2-Cb	AV2-A0			
	Parent magma measured	Daughter magma measured	calculated		
Ba	142	b.d.l.	0.9		
Rb	380	530	524		
Sr	218	7.19	6.8		
Zr	500	1,039	1,028		
La	93	185	170		
Eu	1.97	1.54	1.5		
Th	49	109	102		

Mineral compositions for Averno 2 products are from Civetta et al. (1988)

Major and trace element contents are from Table 2. b.d.l. = below detection limit

Mineral/liquid partition coefficient for the trace element used are from Lemarchand et al. (1987), except those for apatite, from Rollinson (1993) and quoted references

An aerial photographic analysis was carried out in order to identify the main morphological, lithological, and structural features of the Averno area. The results of this analysis were integrated and validated through a field survey. Field work was also carried out on the entire Neapolitan area up to the western margin of the Apennines, aimed at recognizing exposures of the AV2T. Surface data were integrated with borehole data in the Toiano plain, North-East of the Averno lake, in order to complete the stratigraphic reconstruction of the Tephra in an area buried under younger deposits. 33 detailed reconstructions of the internal stratigraphic sequence were performed on the basis of sedimentological characteristics of the deposits and their variation, and occurrence of erosion surfaces. For each deposit thickness, maximum pumice clast and maximum lithic clast, were measured. The investigated sections were correlated by comparing the characteristics of each deposit, and a type sequence was constructed and subdivided in members and sub-members (Figs. 2 and 3).

Table 5 Results of geochemical modeling (Stormer and Nicholls 1978) for the transition from NYT average trachyte to Averno 2 peralkaline alkali-trachyte

Major oxides (wt.%)					
Sample	NYT-trachyte	AV2-A0			
	Parent magma	Daughter magma	Difference between parent and daughter magmas		
	measured	measured	observed	calculated	observed-calculated (residuals)
SiO_2	57.29	61.96	4.67	4.63	0.039
TiO_2	0.53	0.39	-0.14	-0.24	0.103
Al_2O_3	18.35	18.22	-0.13	-0.12	-0.004
Fe_2O_3tot	6.25	3.43	-2.82	-2.83	0.005
MnO	0.12	0.21	0.09	0.10	-0.006
MgO	1.33	0.25	-1.08	-1.07	-0.009
CaO	4.16	1.81	-2.35	-2.32	-0.032
Na_2O	3.62	6.37	2.75	2.84	-0.092
K_2O	8.07	7.29	-0.78	-0.70	-0.075
P_2O_5	0.28	0.07	-0.21	-0.28	0.072
Total	100.00	100.00			
Sum of the squares of residuals					0.033
Subtracted minerals		Amounts relative to initial magma	Absolute amounts		
Sanidine (Or_{77})		51.51	63.02		
Plagioclase (An_{48})		14.35	17.56		
Clinopyroxene ($Wo_{49}Fs_{17}En_{34}$)		8.35	10.21		
Biotite		1.84	2.25		
Ti-magnetite (Usp_{27})		4.88	5.98		
Apatite		0.80	0.98		
Total relative to initial magma		81.74	100.00		
Trace elements (p.p.m.)					
Sample	NYT-trachyte	AV2-A0			
	Parent magma measured	Daughter magma measured	calculated		
Ba	1,192	b.d.l.	1.2		
Rb	307	530	546		
Sr	717	7.19	7.1		
Zr	280	1,039	1,034		
La	73	185	180		
Eu	2.33	1.54	1.58		
Th	27.3	109	116		

Whole rock and mineral compositions for NYT average trachyte are from Orsi et al. (1995)

Major oxide and trace element contents for sample AV2-A0 are from Table 2. b.d.l. = below detection limit

Mineral/liquid partition coefficient for the trace element used are from Lemarchand et al. (1987), except those for apatite, from Rollinson (1993) and quoted references

The maximum lithic clast size and thickness of the fall deposits, measured in the field, have been interpolated to construct isopleths and isopachs maps. Their reconstruction has permitted estimations of the column height and the magma emitted volume (Pyle 1989; Legros 2000). The volume of the different fall deposits of Member A was also calculated using a GIS-assisted method (Dell'Erba 2004). It takes into account both morphology at the time of the eruption and thickness decrease with distance from the eruption vent, and uses the ArcView GIS software for data analysis. The thickness of the fall deposits, measured in the field, has been interpolated to construct distribution maps (isopachs) and their relative TIN (triangulated irregular network). The linear interpolation of the thickness data, represented on semilog plots (ln $T/area^{1/2}$), allowed the estimation of the maximum thickness at the crater and dispersal area (Table 1). The obtained TINs have been converted to GRID (raster format) and subsequently

analyzed with the Spatial Analyst module of the ArcView 3.3 software. The paucity of thickness data for the individual surge deposits of the three members of AV2T did not allow their volume estimation. For this reason the volume of Member A, B and C deposits was calculated using the total thickness of each member, including both surge and fall deposits. This method was already successfully applied to calculate the volume of deposits generated by the Astroni eruptions (Isaia et al. 2004) and during other 15 explosive eruptions occurred since 5 ka in the Campi Flegrei caldera (Orsi et al. 2009).

Rock samples were collected for sedimentological, morphologic and petrological analyses. In particular 19 samples representative of each member and sub-member of the AV2T were analyzed by Scanning Electron Microscope at the Dipartimento Geomineralogico of the University of Bari. For each sample about 100 ash particles with grain-size between 0.090 and 0.125 mm were observed in order to determine qualitatively the surface features i.e. lithology, shape, vesiculation, alteration, presence of fractures etc. with the aim to determine the dominant fragmentation process or processes (Büttner et al. 2002; Dellino et al. 2001; Dellino and La Volpe 1995; Heiken 1974; Heiken and Wohletz 1985; Palladino et al. 2008). Particles were grouped into 3 types, including lithics. The results are reported in the pie charts of Fig. 3.

One hundred one samples from the three members were collected for sedimentological analyses in selected exposures (sections n. 1, 4, 6, 7, 10, 11, 23, 24, 31 and 32 reported on the map of Fig. 2) distributed around the volcano and at variable distance from the vent. Samples represent all the lithotypes described in Figs. 2 and 3. Grain-size analyses were carried out by dry sieving techniques in the size range from -6 to +3 phi, and through Coulter Counter Multisizer in the +3.5 ÷ +6.5 phi range. Results are plotted on diagrams of Fig. 3.

Twelve pumice samples representative of the three members of the AV2T were collected at different localities for mineralogical, petrographic, geochemical and isotopic analyses. Their stratigraphic position is reported on the type section of Figs. 3 and 9. In particular, eight samples are representative of the six recognized coarse-grained fall deposits of Member A, whereas two samples are from coarse-grained pumice deposits interbedded in the surge sequence of Member B, and two more are from Member C. Vesicle and phenocryst percentages were evaluated by combining visual estimations performed both on pumice fragments in the field and on thin section under the microscope. Each sample was composed of several pumice fragments. Prior to powdering, the surface of fragments was treated with a dentist drill equipped with diamond disks in order to remove altered portions. Because of the vicinity of sea to the sampling localities, the fragments were repeatedly washed in abundant de-ionized water to release possible traces of marine salt. Then the samples were dried and ground in an agate mill. Major oxide and trace element contents (Table 2) were determined by ICP-AES (major oxides) and ICP-MS (trace elements) at the Centre de Récherche Pétrographiques et Géochimiques, Nancy (France). Accuracy was checked against International Rock Standards; precision is 1–5% for most major oxides, and <10% for TiO_2 and P_2O_5. The precision of trace element determinations is generally <5% for contents higher than 100 ppm, <10% for contents between 50 and 100 ppm, and <20% for contents between 10 and 1 ppm (S.A.R.M. website: http://crpg.cnrs-nancy.fr/SARM/index.html). $^{87}Sr/^{86}Sr$ and $^{143}Nd/^{144}Nd$ ratios were determined on all bulk rock samples, and separated minerals and glass of several representative samples. Further $^{87}Sr/^{86}Sr$ analyses have been carried out on 6 whole rock samples collected from the sub-member A2, geochemically investigated also by Perugini et al. (2010) in order to integrate our set of isotopic data and better characterize the main compositional variation occurred during the eruption. Sr- and Nd-isotope ratios were measured by thermal ionization mass spectrometry at the Isotope Geochemistry laboratory of the Istituto Nazionale di Geofisica e Vulcanologia—Osservatorio Vesuviano (Naples), using a TRITON TI multi-collector mass spectrometer. Sr and Nd measurements were normalized for mass fractionation effects to $^{86}Sr/^{88}Sr=0.1194$, and to $^{146}Nd/^{144}Nd=0.7219$, respectively. $2\sigma_{mean}$, i.e. the standard error with $N=180$, is better than ±0.000010 for Sr and ±0.000005 for Nd measurements. The mean measured value of $^{87}Sr/^{86}Sr$ for the standard NIST–SRM 987 was 0.710249±0.000014 (2σ, $N=50$); that of $^{143}Nd/^{144}Nd$ for the La Jolla standard was 0.511850± 0.000015 (2σ, $N=25$). The Sr and Nd blanks were negligible for the analyzed samples during the period of measurements. The measured Sr- and Nd-isotope ratios are listed in Table 3.

References

Alessio M, Bella F, Improta S, Belluomini G, Cortesi C, Turi B (1971) University of Rome carbon -14 dates IX. Radiocarbon 13(2):395–411

Arienzo I, Civetta L, Heumann A, Wörner G, Orsi G (2009) Isotopic evidence for open system processes within the Campanian Ignimbrite (Campi Flegrei-Italy) magma chamber. Bull Volcanol 71(3):285–300. doi:10.1007/s00445-008-0223-0

Arienzo I, Moretti R, Civetta L, Orsi G, Papale P (2010) The feeding system of Agnano-Monte Spina eruption (Campi Flegrei, Italy): dragging the past into present activity and future scenarios. Chem Geol 270:135–147. doi:10.1016/j.chemgeo.2009.11.012

Armienti P, Barberi F, Bizouard H, Clocchiatti R, Innocenti F, Métrich N, Rosi M, Sbrana A (1983) The Phlegraean fields: magma

evolution within a shallow chamber. J Volcanol Geotherm Res 17:289–311

Barberi F, Innocenti F, Lirer L, Munno R, Pescatore T, Santacroce R (1978) The Campanian Ignimbrite: a major prehistoric eruption in the Neapolitan area (Italy). Bull Volcanol 41(1):1–22

Boudon G, Komorowski JC, Villemant B, Semet MP (2008) A new scenario for the last magmatic eruption of La Soufrière of Guadeloupe (Lesser Antilles) in 1530 A.D. Evidence from stratigraphy radiocarbon dating and magmatic evolution of erupted products. J Volcanol Geotherm Res 178:474–490

Büttner R, Dellino P, La Volpe L, Lorenz V, Zimanowski B (2002) Thermohydraulic explosions in phreatomagmatic eruptions as evidenced by the comparison between pyroclasts and products from Molten Fuel Coolant Interaction experiments. J Geophys Res 107, B11:pp, doi:10.1029/2001JB000511

Caliro S, Chiodini G, Moretti R, Avino R, Granieri D, Russo M, Fiebig J (2007) The origin of the fumaroles of La Solfatara (Campi Flegrei, South Italy). Geochim Cosmochim Acta 71:3040–3055

Civetta L, Innocenti F, Sbrana A, Taddeucci G (1988) Variazioni petrografiche e geochimiche nei prodotti di Averno: implicazioni sulla zonatura del sistema di alimentazione. Boll Gr Naz Vulcanol IV:201–217

Civetta L, Orsi G, Pappalardo L, Fisher RV, Heiken G, Ort M (1997) Geochemical zoning, mingling, eruptive dynamics and depositional processes—the Campanian Ignimbrite, Campi Flegrei Caldera, Italy. J Volcanol Geotherm Res 75:183–219

Cosentino D, De Rita D, Funiciello R, Parlotto M, Salvini F, Vittori E (1984) Fracture system in Phlegraean Fields (Naples, Southern Italy). Bull Volcanol 47(2):247–258

Costa A, Dell'Erba F, Di Vito M, Isaia R, Macedonio G, Orsi G, Pfeiffer T (2009) Tephra fallout hazard assessment at the Campi Flegrei caldera (Italy). Bull Volcanol 71:259–273. doi:10.1007/s00445-008-0220-3

D'Antonio M, Civetta L, Orsi G, Pappalardo L, Piochi M, Carandente A, de Vita S, Di Vito MA, Isaia R (1999) The present state of the magmatic system of the Campi Flegrei caldera based on a reconstruction of its behavior in the past 12 ka. J Volcanol Geotherm Res 91:247–268

D'Antonio M, Tonarini S, Arienzo I, Civetta L, Di Renzo V (2007) Components and processes in the magma genesis of the Phlegrean Volcanic District, southern Italy. In Beccaluva L, Bianchini G, Wilson M, (eds) Cenozoic volcanism in the Mediterranean area. Geol Soc Am Sp Pap 418:203–220

Deino AL, Orsi G, Piochi M, de Vita S (2004) The age of the Neapolitan Yellow Tuff caldera–forming eruption (Campi Flegrei caldera–Italy) assessed by $^{40}Ar/^{39}Ar$ dating method. J Volcanol Geotherm Res 133:157–170

Dell'Erba F (2004) Definizione dei parametri fisici di alcune eruzioni esplosive della caldera dei Campi Flegrei negli ultimi 15 ka: implicazioni per la valutazione della pericolosità vulcanica. Unpublished PhD thesis

Dellino P, Isaia R, La Volpe L, Orsi G (2001) Statistical analysis of textural data from complex pyroclastic sequence: implication for fragmentation processes of the Agnano-Monte Spina eruption (4.1 ka), Phlegraean Fields, southern Italy. Bull Volcanol 63:443–461

Dellino P, Isaia R, La Volpe L, Orsi G (2004) Interaction between particles transported by fallout and surge in the deposits of the Agnano-Monte Spina eruption (Campi Flegrei, Southern Italy). J Volcanol Geotherm Res 133:193–210

Dellino P, La Volpe L (1995) Fragmentation versus transportation mechanisms in the pyroclastic sequences of Monte Pilato-Rocche Rosse (Lipari, Italy). J Volcanol Geotherm Res 64:211–231

De Lorenzo G (1904) L'attività vulcanica nei Campi Flegrei. Rend Acc Sc Fis Mat Napoli 10:204–221

de Vita S, Orsi G, Civetta L, Carandente A, D'Antonio M, Deino A, di Cesare T, Di Vito MA, Fisher RV, Isaia R, Marotta E, Necco A, Ort M, Pappalardo L, Piochi M, Southon J (1999) The Agnano-Monte Spina eruption (4,100 years BP) in the restless Campi Flegrei caldera (Italy). J Volcanol Geotherm Res 91:269–301

De Vivo B, Rolandi G, Gans PB, Calvert A, Bohrson WA, Spera FJ, Belkin HE (2001) New constraints on the pyroclastic eruptive history of the Campanian volcanic Plain (Italy). Mineral Petrol 73:47–65

Di Girolamo P, Ghiara MR, Lirer L, Munno R, Rolandi G, Stanzione D (1984) Vulcanologia e petrologia dei Campi Flegrei. Boll Soc Geol Ital 103:349–413

Di Renzo V, Arienzo I, Civetta L, D'Antonio M, Tonarini S, Di Vito MA, Orsi G (2010) The magmatic feeding system of the Campi Flegrei caldera: architecture and temporal evolution. Chem Geol, submitted

Di Vito MA, Isaia R, Orsi G, Southon J, de Vita S, D'Antonio M, Pappalardo L, Piochi M (1999) Volcanism and deformation since 12,000 years at the Campi Flegrei caldera (Italy). J Volcanol Geotherm Res 91:221–246

Di Vito MA, Lirer L, Mastrolorenzo G, Rolandi G (1987) The Monte Nuovo eruption (Campi Flegrei, Italy). Bull Volcanol 49:608–615

D'Oriano C, Poggianti E, Bertagnini A, Cioni R, Landi P, Polacci M, Rosi M (2005) Changes in eruptive style during the A.D. 1538 Monte Nuovo eruption (Phlegrean Fields, Italy): the role of syn-eruptive crystallization. Bull Volcanol 67:601–621

Fedele FG, Giaccio B, Isaia R, Orsi G (2002) Ecosystem impact of the Campanian Ignimbrite eruption in Late Pleistocene Europe. Quat Res 57:420–424

Fedele FG, Giaccio B, Isaia R, Orsi G (2003) The Campanian Ignimbrite eruption, Heinrich Event 4, and Palaeolithic change in Europe: a high-resolution investigation. In Robok A, Oppenheimer C (eds), Volcanism and the Earth's Atmosphere. Am Geophys Un, Geophys Monogr 139:301–325

Fedele L, Scarpati C, Lanphere M, Melluso L, Morra V, Perrotta A, Ricci G (2008) The Breccia Museo formation, Campi Flegrei, Southern Italy: geochronology, chemostratigraphy and relationship with the Campanian Ignimbrite eruption. Bull Volcanol 70 (10):1189–1219. doi:10.1007/s00445-008-0197-y

Fisher RV, Orsi G, Ort M, Heiken G (1993) Mobility of a large volume pyroclastic flow emplacement of the Campanian Ignimbrite, Italy. J Volcanol Geotherm Res 56:205–220

Folch A, Martı J (1998) The generation of overpressure in felsic magma chambers by replenishment. Earth Planet Sci Lett 163:301–314

Ghiara MR (1989-90) Studio evolutivo del sistema magmatico flegreo negli ultimi 10 ka. Boll Soc Natur Napoli 98-99:41–70

Heiken G (1974) An atlas of volcanic ash. Smithsonian Contrib Earth Sci 12:1–101

Heiken G, Wohletz K (1985) Volcanic ash. University of California Press, Berkeley, pp 1–246

Isaia R, D'Antonio M, Dell'Erba F, Di Vito M, Orsi G (2004) The Astroni volcano: the only example of closely spaced eruptions in the same vent area during the recent history of the Campi Flegrei caldera (Italy). J Volcanol Geotherm Res 133:171–192

Langmuir CH, Vocke RDJ, Hanson GM, Hart SR (1978) A general mixing equation with application to Icelandic basalts. Earth Planet Sci Lett 37:380–392

Legros F (2000) Minimum volume of tephra fallout deposit estimated from a single isopach. J Volcanol Geotherm Res 96:25–32

Le Maitre RW (1989) In: Bateman P, Dudek A, Keller J, Lameyr J, Le Bas MJ, Sabine PJ, Schmid R, Sörensen H, Streckeisen A, Woolley AR, Zanettin B (eds) A classification of igneous rocks and glossary of terms: recommendations of the international union of geological sciences subcommission on the systematics of igneous rocks. Blackwell, Trowbridge, pp 1–193

Lemarchand F, Villemant B, Calas G (1987) Trace element distribution coefficients in alkaline series. Geochim Cosmochim Acta 51:1071–1081

Lirer L, Di Vito M, Giacomelli L, Scandone R, Vinci A (1990) Contributo delle analisi granulometriche alla ricostruzione della dinamica dell'eruzione di Averno (Campi Flegrei). Boll Soc Geol It 109:583–597

Mangiacapra A, Moretti R, Rutherford M, Civetta L, Orsi G, Papale P (2008) The deep magmatic system of the Campi Flegrei caldera (Italy). Geophys Res Lett 35:L21304

Marianelli P, Sbrana A, Proto M (2006) Magma chamber of the Campi Flegrei supervolcano at the time of eruption of the Campanian Ignimbrite. Geology 34(11):937–940

Mastrolorenzo G (1994) Averno tuff ring in Campi Flegrei (South Italy). Bull Vulcanol 56:561–572

Mastrolorenzo G, Pappalardo L, Troise C, Panizza A, De Natale G (2008) Probabilistic tephra hazard maps for the Neapolitan area: quantitative volcanological study of Campi Flegrei eruptions. J Geophys Res 113:B07203. doi:10.1029/2007JB004954

Middlemost EAK (1989) Iron oxidation ratios, norms and the classification of volcanic rocks. Chem Geol 77:19–26

Morgan DJ, Davidson JP, Pearson DG, Nowell GM, Civetta L (2004) Strontium isotopic heterogeneity among phenocrysts of the Minopoli 2 eruption of the Campi Flegrei caldera complex (9500 BP). Geophys Res Abstr 6:04003

Murphy MD, Sparks RSJ, Barclay J, Carroll MR, Brewer TS (2000) Remobilization of andesite magma by intrusion of mafic magma at the Soufriere Hills volcano, Montserrat, West Indies. J Petrol 41:21–42

Murphy MD, Sparks RSJ, Barclay J, Carroll MR, Lejeune A-M, Brewer TS, Macdonald R, Black S, Young S (1998) The role of magma mixing in triggering the current eruption at the Soufriere Hills Volcano, Montserrat, West Indies. Geophys Res Lett 25 (18):3,433–3,436

Orsi G, Civetta L, D'Antonio M, Di Girolamo P, Piochi M (1995) Step-filling and development of a three layer magma chamber: the Neapolitan Yellow Tuff case history. J Volcanol Geotherm Res 67:291–312

Orsi G, Civetta L, Del Gaudio C, de Vita S, Di Vito MA, Isaia R, Petrazzuoli S, Ricciardi G, Ricco C (1999a) Short-term ground deformations and seismicity in the nested Campi Flegrei Caldera (Italy): an example of active block resurgence in a densely populated area. J Volcanol Geotherm Res 91:415–451

Orsi G, D'Antonio M, de Vita S, Gallo G (1992) The Neapolitan Yellow Tuff, a large-magnitude trachytic phreatoplinian eruption: eruptive dynamics, magma withdrawal and caldera collapse. J Volcanol Geotherm Res 53:275–287

Orsi G, de Vita S, Di Vito M (1996) The restless, resurgent Campi Flegrei nested caldera (Italy): constraints on its evolution and configuration. J Volcanol Geotherm Res 74:179–214

Orsi G, de Vita S, Di Vito M, Nave R, Heiken G (2003) Facing volcanic and related hazards in the Neapolitan area. In: Heiken G, Fakundiny R, Sutter J (eds) Earth sciences in the cities: a reader. AGU Sp Publ Series 56, Washington, pp 121–170

Orsi G, Di Vito MA, Isaia R (2004) Volcanic hazard assessment at the restless Campi Flegrei caldera. Bull Volcanol 66:514–530

Orsi G, Di Vito MA, Selva J, Marzocchi W (2009) Long-term forecast of eruption style and size at Campi Flegrei caldera (Italy). Earth Planet Sci Lett 287:265–276. doi:10.1016/j.epsl.2009.08.013

Orsi G, Petrazzuoli S, Wohletz K (1999b) Mechanical and thermo-fluid behaviour during unrest episode at the Campi Flegrei caldera (Italy). J Volcanol Geotherm Res 91:453–470

Ort M, Orsi G, Pappalardo L, Fisher RV (2003) Anisotropy of magnetic susceptibility studies of depositional processes in the Camanian Ignimbrite, Italy. Bull Volcanol 65:55–72

Palladino DM, Simei S, Kyriakopoulos K (2008) On magma fragmentation by conduit shear stress: evidence from the Kos Plateau Tuff, Aegean Volcanic Arc. Kos J Volcanol Geotherm Res 178:807–817

Pappalardo L, Civetta L, D'Antonio M, Deino A, Di Vito M, Orsi G, Carandente A, de Vita S, Isaia R, Piochi M (1999) Chemical and Sr–isotopical evolution of the Phlegraean magmatic system before the Campanian Ignimbrite and the Neapolitan Yellow Tuff eruptions. J Volcanol Geotherm Res 91:141–166

Pappalardo L, Civetta L, de Vita S, Di Vito M, Orsi G, Carandente A, Fisher RV (2002a) Timing of magma extraction during the Campanian Ignimbrite eruption (Campi Flegrei Caldera). J Volcanol Geotherm Res 114:479–497

Pappalardo L, Piochi M, D'Antonio M, Civetta L, Petrini R (2002b) Evidence for multi-stage magmatic evolution during the past 60 kyr at Campi Flegrei (Italy) deduced from Sr, Nd and Pb isotope data. J Petrol 43:1415–1434

Perugini D, Poli G, Petrelli M, De Campos CP, Dingwell DB (2010) Time-scales of recent Phlegrean Fields eruptions inferred from the application of a 'diffusive fractionation' model of trace elements. Bull Volcanol 72(4):431–447

Piochi M, Mastrolorenzo G, Pappalardo L (2005) Magma ascent and eruptive processes from textural and compositional features of Monte Nuovo pyroclastic products, Campi Flegrei, Italy. Bull Volcanol 67:663–678

Pyle DM (1989) The thickness, volume and grain size of tephra fall deposits. Bull Volcanol 51:1–15

Pyle DM (1995) Assessment of the minimum volume of tephra fall deposits. J Volcanol Geotherm Res 69:379–382

Pyle DM (2000) Sizes of volcanic eruptions. Encyclopedia of volcanoes, Academic Press 263–269

Rittmann A (1950) Sintesi geologica dei Campi Flegrei. Boll Soc Geol It 69:117–128

Rollinson H (1993) Using geochemical data: evaluation, presentation, interpretation. Prentice Hall, England, pp 1–352

Rosi M, Sbrana A (1987) The Phlegrean fields. Quad Ric Sci CNR, Rome, pp 1–175

Rosi M, Vezzoli L, Aleotti P, De Cenzi M (1996) Interaction between caldera collapse and eruptive dynamics during the Campanian Ignimbrite eruption, Phlegraean Fields, Italy. Bull Volcanol 57:541–554

Rosi M, Vezzoli L, Castelmenzano A, Grieco G (1999) Plinian pumice fall deposit of the Campanian Ignimbrite eruption (Phlegraean Fields, Italy). J Volcanol Geotherm Res 91:179–198

Santacroce R, Cristofolini R, La Volpe L, Orsi G, Rosi M (2003) Italian active volcanoes. Episodes 26(3):227–234

Scarpati C, Cole P, Perrotta A (1993) The Neapolitan Yellow Tuff—a large volume multiphase eruption from Campi Flegrei, Southern Italy. Bull Volcanol 55:343–356

Scherillo A, Franco E (1960) Rilevamento stratigrafico del territorio comunale di Napoli. Boll Soc Natur Napoli LXIX:255–262

Schmitz MD, Smith IEM (2004) The petrology of the Rotoiti eruption sequence, Taupo Volcanic Zone: an example of fractionation and mixing in a rhyolitic system. J Petrol 45(10):2045–2066

Selva J, Orsi G, Di Vito MA, Marzocchi W, Sandri L (2010) Probability hazard map for future vent opening at the Campi Flegrei caldera, Italy. Bull Volcanol submitted

Sparks SRJ, Sigurdsson H, Wilson L (1977) Magma mixing-mechanism for triggering acid explosive eruptions. Nature 267:315–318

Stormer JC, Nicholls J (1978) XLFrac: a program for the interactive testing of magmatic differentiation models. Comp Geosci 4:143–159

Thornton CP, Tuttle OF (1960) Chemistry of igneous rocks. I. Differentiation Index. Am J Sci 258:664–684

Tonarini S, D'Antonio M, Di Vito MA, Orsi G, Carandente A (2009) Geochemical and B-Sr-Nd isotopic evidence for mingling and mixing processes in the magmatic system that fed the Astroni

volcano (4.1-3.8 ka) within the Campi Flegrei caldera (southern Italy). Lithos 107:135–151

Tonarini S, Leeman WP, Civetta L, D'Antonio M, Ferrara G, Necco A (2004) B/Nb and $\delta^{11}B$ systematics in the Phlegrean Volcanic District, Italy. J Volcanol Geotherm Res 133:123–139

Wilson L, Walker GPL (1987) Explosive volcanic eruptions–VI. Ejecta dispersal in plinian eruptions, the control of eruption conditions and atmospheric properties. Geophys J R Astron Soc 89:657–679

Wohletz K, Orsi G, de Vita S (1995) Eruptive mechanisms of the Neapolitan Yellow Tuff interpreted from stratigraphic, chemical and granulometric data. J Volcanol Geotherm Res 67:263–290

Zollo A, Maercklin N, Vassallo M, Dello Iacono D, Virieux J, Gasparini, P (2008) Seismic reflections reveal a massive melt layer feeding Campi Flegrei caldera. Geophys Res Lett 35 L12306 doi:10.1029/2008GL034242